

1                   **Rheologic constraints on the upper mantle from five years of**  
2                   **postseismic deformation following the El Mayor-Cucapah**  
3                   **earthquake**

4                   **T. T. Hines<sup>1</sup>, E. A. Hetland<sup>1</sup>**

5                   <sup>1</sup>Department of Earth and Environmental Sciences, University of Michigan, Ann Arbor, Michigan, USA.

6                   **Key Points:**

- 7                   • Transient postseismic deformation can be observed following the El Mayor-Cucapah  
8                   earthquake at epicentral distances of up to 400 km  
9                   • Near-field postseismic deformation exhibits early transience that decays to a sustained  
10                  rate which is elevated above the preseismic trend  
11                  • A Zener or Burgers upper mantle can explain far-field deformation while near-field tran-  
12                  sience can be described with afterslip

13 **Abstract**

14 Five years of postseismic deformation following the Mw=7.2 El Mayor-Cucapah earthquake  
 15 reveals transient deformation that decays back to its pre-earthquake trend after about three years  
 16 at epicentral distances greater than  $\sim 200$  km. At shorter distances, the rapid transience decays  
 17 to a sustained rate which exceeds its pre-earthquake trend. We attempt to determine the mech-  
 18 anisms driving this deformation, where we consider afterslip at seismogenic depths and vis-  
 19 coelastic relaxation in the lower crust and upper mantle as candidate mechanisms. We find that  
 20 early, rapid, near-field deformation can be explained with afterslip on the fault that ruptured  
 21 coseismically, while the later, sustained, near-field deformation can be explained with either  
 22 continued afterslip in an effectively elastic lower crust, or lower crustal viscoelastic relaxation  
 23 with a steady-state viscosity of  $\sim 10^{19}$  Pa s. The trend in far-field deformation is best explained  
 24 with a transient viscosity of  $\sim 10^{18}$  Pa s in the upper mantle. We argue that a transient rhe-  
 25 ology in the mantle is preferable over a Maxwell rheology because it better predicts the de-  
 26 cay in postseismic deformation, and also because it does not conflict with the generally higher,  
 27 steady-state viscosities inferred from studies of geophysical processes occurring over longer  
 28 time-scales.

29 **1 Introduction**

30 Ground deformation in the years following a large ( $\gtrsim$ Mw7) earthquake can be used to  
 31 gain insight into the mechanical behavior of the crust and upper mantle. The interpretations  
 32 of postseismic deformation are not always conclusive because multiple postseismic deforma-  
 33 tion mechanisms, such as afterslip or viscoelastic relaxation in the lower crust and upper man-  
 34 tle, can have qualitatively similar surface expressions [e.g. Savage, 1990]. This complication  
 35 can potentially be remedied by having a sufficient number of well positioned observations of  
 36 the postseismic displacement field [Hearn, 2003]. Owing to the dense geodetic network de-  
 37 ployed throughout the 2000s as part of the Plate Boundary Observatory, the postseismic de-  
 38 formation following the April 4, 2010, Mw7.2 El Mayor-Cucapah earthquake in Baja Cali-  
 39 fornia was observed at more GPS stations than any other earthquake in California to date. With  
 40 such a large collection of data, we attempt to discern the mechanisms driving postseismic de-  
 41 formation following the El Mayor-Cucapah earthquake.

42 Here is some background on the El Mayor Earthquake

43 Previous studies which have modeled postseismic deformation following the El Mayor-  
 44 Cucapah earthquake include Pollitz *et al.* [2012], Gonzalez-Ortega *et al.* [2014], Spinler *et al.*  
 45 [2015], and Rollins *et al.* [2015]. Of these studies, Gonzalez-Ortega *et al.* [2014] and Rollins  
 46 *et al.* [2015] have attempted to describe the postseismic deformation with afterslip in an elas-  
 47 tic half-space. Gonzalez-Ortega *et al.* [2014] described five months of postseismic deforma-  
 48 tion, observed by InSAR and GPS within  $\sim 50$  km of the rupture, with afterslip and contrac-  
 49 tion on the coseismically ruptured fault. Gonzalez-Ortega *et al.* [2014] noted that their preferred  
 50 model underestimated the GPS displacements for stations  $\gtrsim 25$  km from the rupture and sug-  
 51 gested that it could be the result of unmodeled viscoelastic relaxation. Using only continuous  
 52 GPS stations, which are mostly north of the rupture zone, Rollins *et al.* [2015] found that three  
 53 years of postseismic deformation can be adequately explained by afterslip, albeit with an im-  
 54 plausibly large amount of slip inferred on the least constrained, southern-most fault segment.  
 55 Here, we suggest the afterslip inferred by Rollins *et al.* [2015] may have been acting as a proxy  
 56 for distributed relaxation in the upper mantle.

57 Pollitz *et al.* [2012], Rollins *et al.* [2015] and Spinler *et al.* [2015] have explored viscoelas-  
 58 tic relaxation in the lower crust and upper mantle as a potential postseismic deformation mech-  
 59 anism. The rheology of the crust and mantle is largely unknown and so modeling postseis-  
 60 mic deformation with viscoelastic relaxation requires one to assume a rheologic model and  
 61 then find the best fitting rheologic parameters. The inference of these rheologic parameters is  
 62 a computationally expensive non-linear inverse problem which is typically approached with  
 63 a forward modeling grid search method. Consequently, a simplified structure for the Earth must

be assumed in order to minimize the number of rheologic parameters that need to be estimated. For example, it is commonly assumed that the lower crust and upper mantle are homogeneous, Maxwell viscoelastic layers, which may be too simplistic for postseismic studies [Riva and Govers, 2009; Hines and Hetland, 2013]. To further reduce the dimensions of the model space, it is also necessary to make simplifying assumptions about the behavior of afterslip. For example, one can assume a frictional model for afterslip and parametrize afterslip in terms of the unknown rheologic properties of the fault [e.g. Johnson *et al.*, 2009; Johnson and Segall, 2004]. One can also assume that afterslip does not persist for more than a few months and then model the later postseismic deformation assuming it to be the result of only viscoelastic relaxation [e.g. Pollitz *et al.*, 2012; Spinler *et al.*, 2015]. However, postseismic afterslip in similar tectonic settings has been observed to persist for decades following earthquakes [Cakir *et al.*, 2012; Cetin *et al.*, 2014]. Indeed, the preferred viscoelastic model from Pollitz *et al.* [2012] significantly underestimates deformation in the Imperial Valley, which could be indicative of unmodeled continued afterslip. Neglecting to allow for sustained afterslip as a postseismic mechanism could then lead to biased inferences of viscosities.

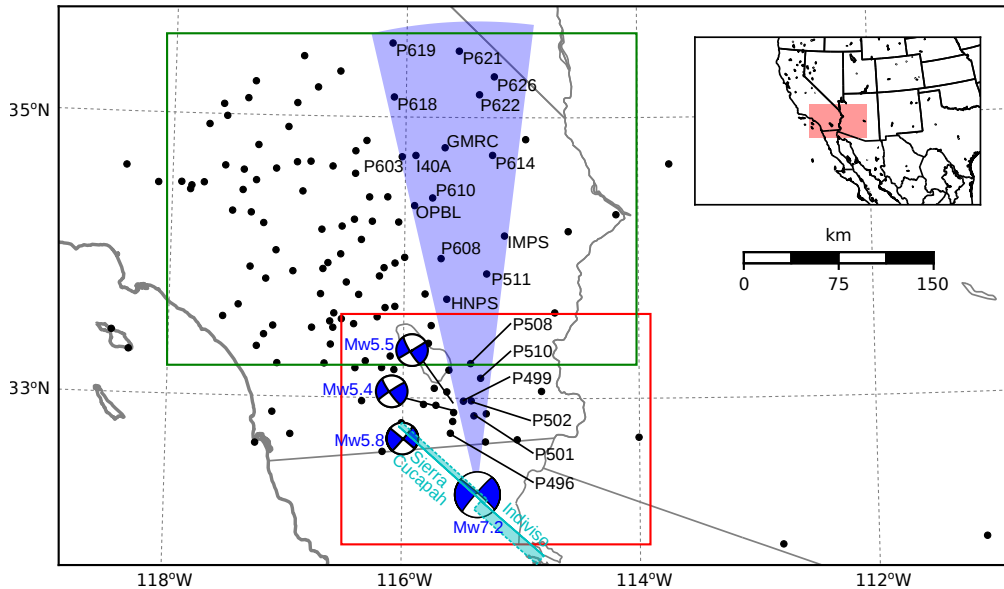
In this study, we perform a kinematic inversion for fault slip, allowing it to persist throughout the postseismic period, while simultaneously estimating the viscosity of the lower crust and upper mantle. We create an initial model of the fault slip and effective viscosity necessary to describe early postseismic deformation using the method described in Hines and Hetland [2016]. This method utilizes a first-order approximation of surface deformation resulting from viscoelastic relaxation which is only applicable to the early postseismic period. In this case, our initial model describes the first 0.8 years of postseismic deformation following the El Mayor-Cucapah earthquake. We then use the inferred effective viscosity structure from the initial model to create a suite of postseismic models to explain the five years of postseismic data available to date. Of the suite of models tested, we find that postseismic deformation following the El Mayor-Cucapah earthquake can be explained with a combination of afterslip on a fault segment running through the Sierra Cucapah and a Zener rheology in the upper mantle with a transient viscosity that decays from  $6 \times 10^{18}$  Pa s to  $1 \times 10^{18}$  Pa s at 120 km depth.

## 2 Data Processing

We use continuous GPS position time series provided by University Navstar Consortium (UNAVCO) for stations within a 400 km radius about the El Mayor-Cucapah epicenter. We collectively describe the coseismic and postseismic displacements resulting from the El Mayor-Cucapah earthquake as  $u_{\text{post}}(t)$ . We consider the GPS position time series  $u_{\text{obs}}(t)$  to be the combination of  $u_{\text{post}}(t)$ , secular tectonic deformation, annual and semi-annual oscillations, and coseismic offsets from significant earthquakes over the time span of this study. The June 14, 2010, Mw5.8 Ocotillo earthquake and the Brawley swarm, which included an Mw5.5 and an Mw5.4 event on August 26, 2012, (Figure 1) are the only earthquakes that produced noticeable displacements in any of the time series. We treat the displacements resulting from the Brawley swarm as a single event because the daily solutions provided by UNAVCO cannot resolve the separate events. Although the Ocotillo earthquake had its own series of aftershocks [Hauksson *et al.*, 2011], neither the Ocotillo earthquake nor the Brawley swarm produced detectable postseismic deformation. We model displacements resulting from these events with only a Heaviside function,  $H(t)$ , describing the coseismic offsets. We then model  $u_{\text{obs}}(t)$  as

$$u_{\text{obs}}(t) = u_{\text{pred}}(t) + \epsilon, \quad (1)$$

where



93 **Figure 1.** Map of the region considered in this study. The large focal mechanism is for the El Mayor-  
94 Cucapah earthquake, and the three small focal mechanisms are for the Ocotillo earthquake and the two main  
95 shocks during the Brawley swarm. The black dots indicate the locations of GPS stations used in this study.  
96 The fault geometry used in this study is shown in cyan where dashed lines indicate buried edges of the fault  
97 segments. The green and red boxes demarcate the extent of the near-field and far-field maps (Figures 4 and 5).  
98 Stations inside the blue sector, which highlights the area within  $10^\circ$  of the El Mayor-Cucapah P axis, are used  
99 in Figures 7, 10, and 14

$$\begin{aligned} u_{\text{pred}}(t) = & u_{\text{post}}(t)H(t - t_{\text{emc}}) + c_0 + c_1t + \\ & c_2 \sin(2\pi t) + c_3 \cos(2\pi t) + c_4 \sin(4\pi t) + c_5 \cos(4\pi t) + \\ & c_6 H(t - t_{\text{oc}}) + c_7 H(t - t_{\text{bs}}). \end{aligned} \quad (2)$$

In the above equations,  $t_{\text{emc}}$ ,  $t_{\text{oc}}$  and  $t_{\text{bs}}$  are the times of the El Mayor-Cucapah earthquake, Ocotillo earthquake, and the Brawley swarm, respectively,  $c_0$  through  $c_7$  are unknown coefficients, and  $\epsilon$  is the observation noise. We only estimate jumps associated with the Ocotillo earthquake and Brawley swarm for stations within 40 km of their epicenters.

Stations which recorded displacements that clearly cannot be described by the aforementioned processes are not included in our analysis. This includes stations in the Los Angeles basin, where anthropogenic deformation can be larger than the postseismic signal that we are trying to estimate [Bawden *et al.*, 2001; Argus *et al.*, 2005]. In order to ensure an accurate estimation of the secular deformation, we only use stations that were installed at least six months prior to El Mayor-Cucapah earthquake. Several GPS stations were installed after the El Mayor-Cucapah earthquake to improve the spatial resolution of postseismic deformation [Spinler *et al.*, 2015]. Although it would be possible to subtract secular velocities derived from elastic block models [e.g. Meade and Hager, 2005] from velocities recorded at the newly installed stations to get an estimate of postseismic velocities, we do not do so here. We use coseismic and postseismic displacements, rather than velocities, in our inverse method described in Section 3. We use displacements because estimating velocities from an already noisy displacement time series can introduce significant uncertainties depending on exactly how the estimation is done. This choice prevents us from using the newly installed stations in Baja California for our analysis.

The October 16, 1999, Mw7.1 Hector Mine earthquake, which occurred  $\sim$ 270 km north of the El Mayor-Cucapah epicenter, produced transient postseismic deformation which we do not wish to model, either mechanically or through empirical line fitting. We thus restrict our analysis to deformation observed six years after the Hector Mine earthquake, which is when postseismic velocities at sites proximal to the Hector Mine epicenter are approximately constant [Savage and Svart, 2009]. When appraising our model fit in Section 3, we see some systematic residuals in the vicinity of the Hector Mine epicenter, which may be the result of errors in the assumption that the trend in Hector Mine postseismic deformation is linear after six years.

Studies of postseismic deformation typically assume a parametric form for  $u_{\text{post}}(t)$ , such as one with a logarithmic or exponential time dependence [e.g. Savage *et al.*, 2005]. However, by assuming a logarithmic or exponential form of  $u_{\text{post}}(t)$  we run the risk of over fitting the GPS time series and inferring a non-existent postseismic signal. We therefore do not assume any parametric form for  $u_{\text{post}}(t)$  and rather treat it as integrated Brownian motion, so that

$$\dot{u}_{\text{post}}(t) = \sigma^2 \int_0^t w(s)ds, \quad (3)$$

where  $w(t)$  is white noise and the variance of  $\dot{u}_{\text{post}}(t)$  increases linearly with time by a factor of  $\sigma^2$ . We use a Kalman filtering approach to estimate  $u_{\text{post}}(t)$  and the unknown parameters in eq. (2). In the context of Kalman filtering, our time varying state vector is

$$\mathbf{X}(t) = [u_{\text{post}}(t), \dot{u}_{\text{post}}(t), c_0, \dots, c_7] \quad (4)$$

and eq. (2) is the observation function which maps the state vector to the GPS observations. We initiate the Kalman filter by assuming a prior estimate of  $\mathbf{X}(t)$  at the first time epoch, denoted  $\mathbf{X}_{1|0}$ , which has a sufficiently large covariance, denoted  $\Sigma_{1|0}$ , to effectively make our prior uninformed. For each time epoch  $t_i$ , Bayesian linear regression is used to incorporate GPS derived estimates of displacement with our prior estimate of the state  $\mathbf{X}_{i|i-1}$  to form a

157 posterior estimate of the state  $\mathbf{X}_{i|i}$ , which has covariance  $\Sigma_{i|i}$ . We then use the posterior es-  
 158 timate of the state at time  $t_i$  to form a prior estimate of the state at time  $t_{i+1}$  through the trans-  
 159 sition function

$$\mathbf{X}_{i+1|i} = \mathbf{F}_{i+1}\mathbf{X}_{i|i} + \delta_{i+1}, \quad (5)$$

160 where

$$\mathbf{F}_{i+1} = \begin{bmatrix} 1 & (t_{i+1} - t_i) & \mathbf{0} \\ 0 & 1 & \mathbf{0} \\ \mathbf{0} & \mathbf{0} & \mathbf{I} \end{bmatrix} \quad (6)$$

161 and  $\delta_{i+1}$  is the process noise, which has zero mean and covariance described by

$$\mathbf{Q}_{i+1} = \sigma^2 \begin{bmatrix} \frac{(t_{i+1} - t_i)^3}{3} & \frac{(t_{i+1} - t_i)^2}{2} & \mathbf{0} \\ \frac{(t_{i+1} - t_i)^2}{2} & (t_{i+1} - t_i) & \mathbf{0} \\ \mathbf{0} & \mathbf{0} & \mathbf{0} \end{bmatrix}. \quad (7)$$

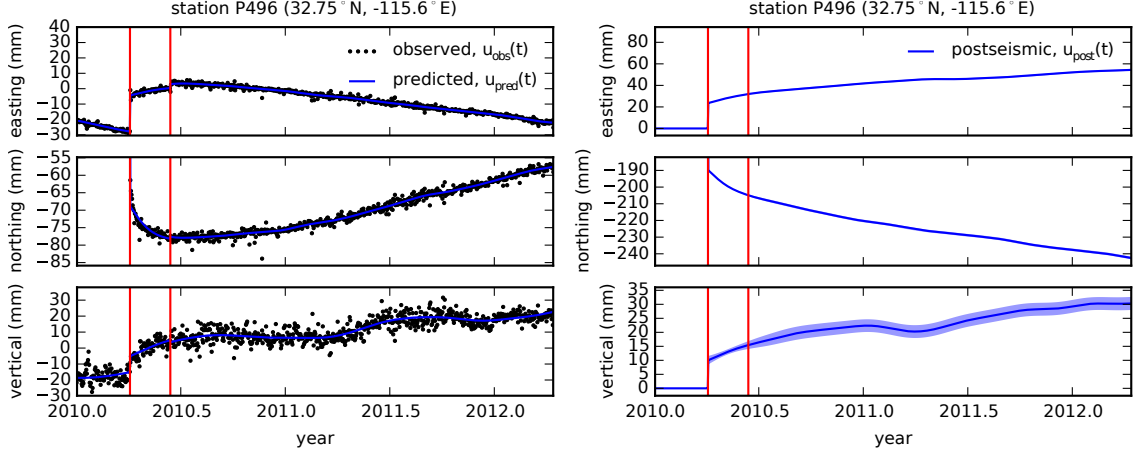
162 The covariance of the new prior state,  $\mathbf{X}_{i+1|i}$ , is then described by

$$\Sigma_{i+1|i} = \mathbf{F}_{i+1}\Sigma_{i|i}\mathbf{F}_{i+1}^T + \mathbf{Q}_{i+1}. \quad (8)$$

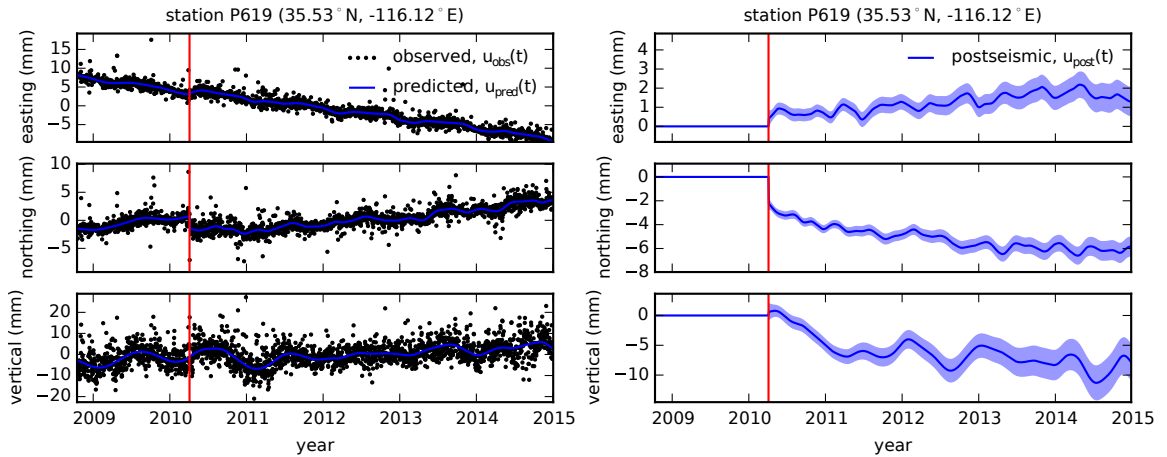
163 This process is repeated for each of the  $N$  time epochs at which point we use Rauch-Tung-  
 164 Striebel smoothing [Rauch *et al.*, 1965] to find  $\mathbf{X}_{i|N}$ , which is an estimate of the state at time  
 165  $t_i$  that incorporates GPS observation for all  $N$  time epochs. Our final estimates of  $u_{\text{post}}(t)$   
 166 are used in subsequent analysis, while the remaining components of the state vector are con-  
 167 sidered nuisance parameters. In the interests of computational tractability, we down sample  
 168 our smoothed time series from daily solutions down to weekly solutions.

169 The smoothness of  $u_{\text{post}}(t)$  is controlled by the chosen value of  $\sigma^2$ , which describes how  
 170 rapidly we expect postseismic displacements to vary over time. Setting  $\sigma^2$  equal to zero will  
 171 effectively result in modeling  $u_{\text{post}}(t)$  as a straight line which is insufficient to describe the  
 172 expected transient behavior in postseismic deformation. The other end member, where  $\sigma^2$  is  
 173 infinitely large, will result in  $u_{\text{pred}}(t)$  over fitting the data. While one can use a maximum like-  
 174 lihood based approach for picking  $\sigma^2$  [e.g. Segall and Mathews, 1997], we instead take a sub-  
 175 jective approach and choose a value for  $\sigma^2$  that is just large enough to faithfully describe the  
 176 observed deformation at the most near-field station in our study, P496, which exhibits the most  
 177 rapid changes in velocity. This ensures that  $\sigma^2$  will be sufficiently large so that our estimate  
 178 of  $u_{\text{post}}(t)$  does not smooth out potentially valuable postseismic signal at the remaining sta-  
 179 tions. We find that using  $\sigma^2 = 0.05\text{m}^2/\text{yr}^3$  adequately describe all but the first week of post-  
 180 seismic deformation at station P496, which gets incorporated into our estimate of coseismic  
 181 displacements (Figure 2). We assume that the first week of deformation is overwhelmingly the  
 182 result of afterslip and this afterslip is lumped into our estimates of coseismic slip. Freed *et al.*  
 183 [2007] noted that postseismic deformation can be observed at distances greater than 200 km  
 184 from the Hector Mine earthquake and, after filtering the time series for stations up to 400 km  
 185 from the El Mayor-Cucapah epicenter, we also clearly see far reaching postseismic transient  
 186 deformation (Figure 3).

187 It is important to note that the shown uncertainties in  $u_{\text{post}}(t)$  do not account for the non-  
 188 negligible epistemic uncertainty in eq. (2). For example, we assume a constant rate of secu-  
 189 lar deformation, which appears to be an appropriate approximation for all but perhaps the sta-  
 190 tions closest to the Hector Mine epicenter, as noted above. Also, our model for seasonal de-  
 191 formation in eq. (2) assumes a constant amplitude over time, which means that any yearly vari-  
 192 ability in the climatic conditions could introduce systematic residuals [Davis *et al.*, 2012]. In-  
 193 deed, it would be more appropriate to consider the seasonal amplitudes  $c_2 - c_5$  in eq. (2) as



187 **Figure 2.** Left panels show GPS time series from UNAVCO (black) and the predicted displacement (blue)  
 188 from eq. (2) for a near-field station. Red lines indicate the times of the El Mayor-Cucapah and Ocotillo earth-  
 189 quakes. The right panels show estimated coseismic and postseismic displacements  $u_{\text{post}}$  which are extracted  
 190 from the predicted displacements. The 68% confidence interval is shown in light blue.



191 **Figure 3.** same as Figure 2 but for a far-field station.

depth (km)	$\lambda$ (GPa)	$\mu$ (GPa)	$\eta_{\text{eff}}$ ( $10^{18}$ Pa s)	$\mu_k/\mu$
0-5	24.0	24.0	-	-
5-15	35.0	35.0	-	-
15-30	42.0	42.0	44.3	0.0
30-60	61.0	61.0	5.91	0.375
60-90	61.0	61.0	1.99	0.375
90-120	61.0	61.0	1.31	0.375
120-150	61.0	61.0	1.10	0.375
150- $\infty$	61.0	61.0	1.07	0.375

231 **Table 1.** Assumed and estimated material properties.  $\lambda$  and  $\mu$  are assumed known *a priori* and are based  
 232 on the values used for the coseismic model by Wei *et al.* [2011b]. The values for  $\eta_{\text{eff}}$  are estimated in Section  
 233 3.2, and  $\frac{\mu_k}{\mu}$  are the optimal shear moduli ratios found in Section 3.3 for a Zener rheology upper mantle.

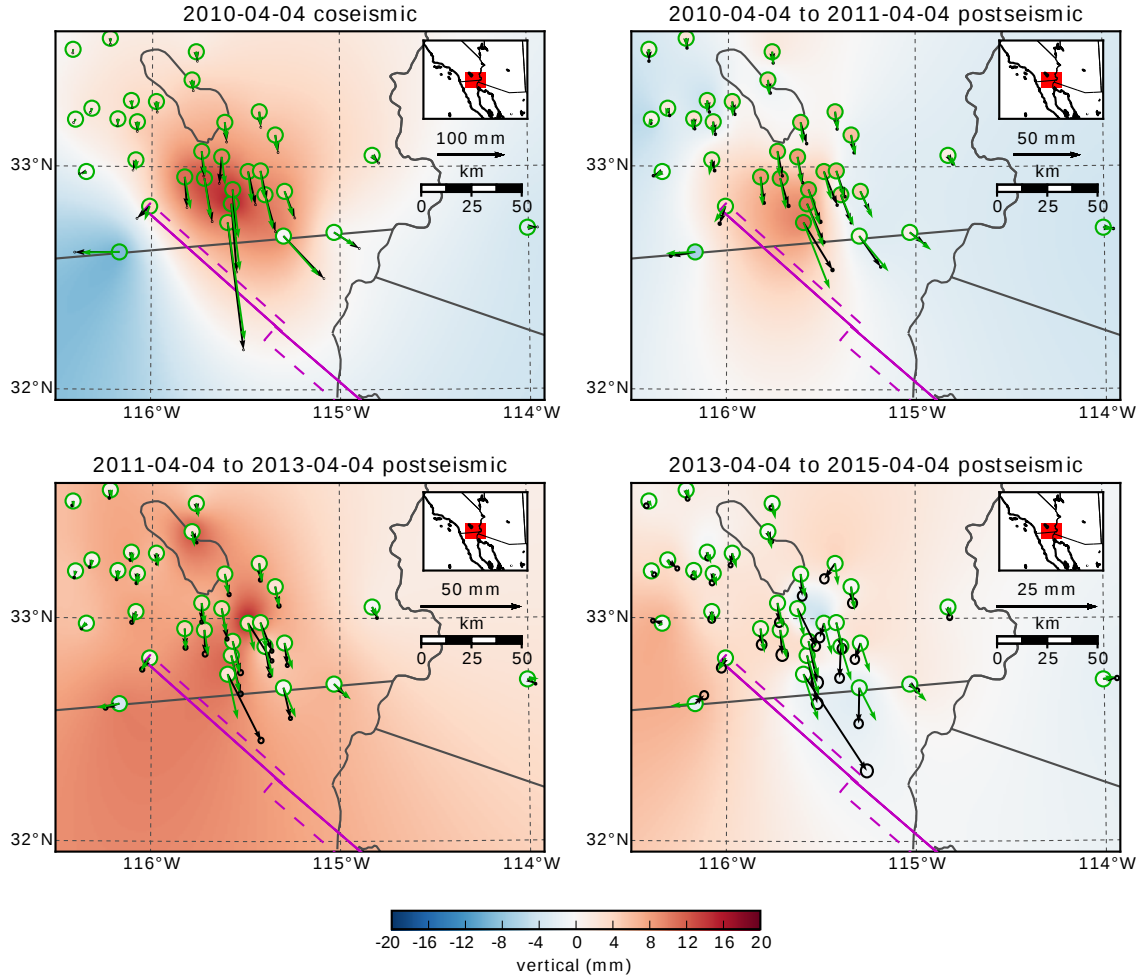
199 stochastic variables [Murray and Segall, 2005]. By using constant seasonal amplitudes, our es-  
 200 timate of  $u_{\text{post}}(t)$  seems to describe some of the unmodeled annual and semi-annual oscilla-  
 201 tions (e.g. Figure 3).

202 We show in Figures 4 and 5 the near and far-field postseismic displacements accumu-  
 203 lated over the time intervals 0-1 years, 1-3 years, and 3-5 years, as well as the coseismic dis-  
 204 placements. Stations at epicentral distances beyond  $\sim 200$  km have an elevated rate of defor-  
 205 mation for the first three years following the earthquake. This far-field deformation has a south-  
 206 ward trend along the direction of the El Mayor-Cucapah P axis and a similar eastward trend  
 207 can be seen in the few far-field stations in Arizona, located along the T axis. After three years,  
 208 the trend in far-field postseismic deformation is barely perceptible. Most far-field stations dis-  
 209 play an initial subsidence for the first year after the El Mayor-Cucapah earthquake followed  
 210 by continued uplift. This trend in vertical deformation can be observed in all three of the quad-  
 211 rants where postseismic data is available, which means that the vertical deformation does not  
 212 exhibit an anti-symmetric quadrant pattern, as would be expected for postseismic processes.  
 213 Although we use vertical deformation in our analysis in Section 3, we do not put an empha-  
 214 sis on trying to describe the vertical deformation as it likely does not have postseismic ori-  
 215 gins.

222 The near-field postseismic deformation is notably sustained when compared to the far-  
 223 field deformation. Namely, the station in this study which is closest to the El Mayor-Cucapah  
 224 epicenter, P496, has a steady postseismic trend of  $\sim 1.5$  cm/yr to the south after about one year.  
 225 Vertical postseismic deformation in the near-field does display a quadrant pattern which is con-  
 226 sistent with the coseismic vertical deformation, suggesting that it is resulting from postseis-  
 227 mic processes. However, the vertical postseismic signal is only apparent for the first year af-  
 228 ter the earthquake (Figure 4). As with the far-field deformation, there is a general trend of up-  
 229 lift in the near-field after about one year.

### 230 3 Postseismic Modeling

234 We seek to find the mechanisms driving five years of postseismic deformation follow-  
 235 ing the El Mayor-Cucapah earthquake and we consider afterslip and viscoelastic relaxation as  
 236 candidate mechanisms. Poroelastic rebound has also been used to model postseismic defor-  
 237 mation [e.g. Jónsson *et al.*, 2003]; however, Gonzalez-Ortega *et al.* [2014] found that poroe-  
 238 lastic rebound is unlikely to be a significant contributor to postseismic deformation following  
 239 the El Mayor-Cucapah earthquake. Furthermore, we consider stations which are sufficiently  
 240 far away from the main rupture that poroelastic rebound should be insignificant.



216 **Figure 4.** Near-field coseismic and cumulative postseismic displacements over the indicated time periods  
 217 (black) as well as predicted displacements for our preferred model from Section 3.3 (green). Observed verti-  
 218 cal deformation is shown as an interpolated field and predicted vertical displacements are shown within the  
 219 circles at the base of each vector. Note that the interpolant is not well constrained in Mexico where there is no  
 220 data available.

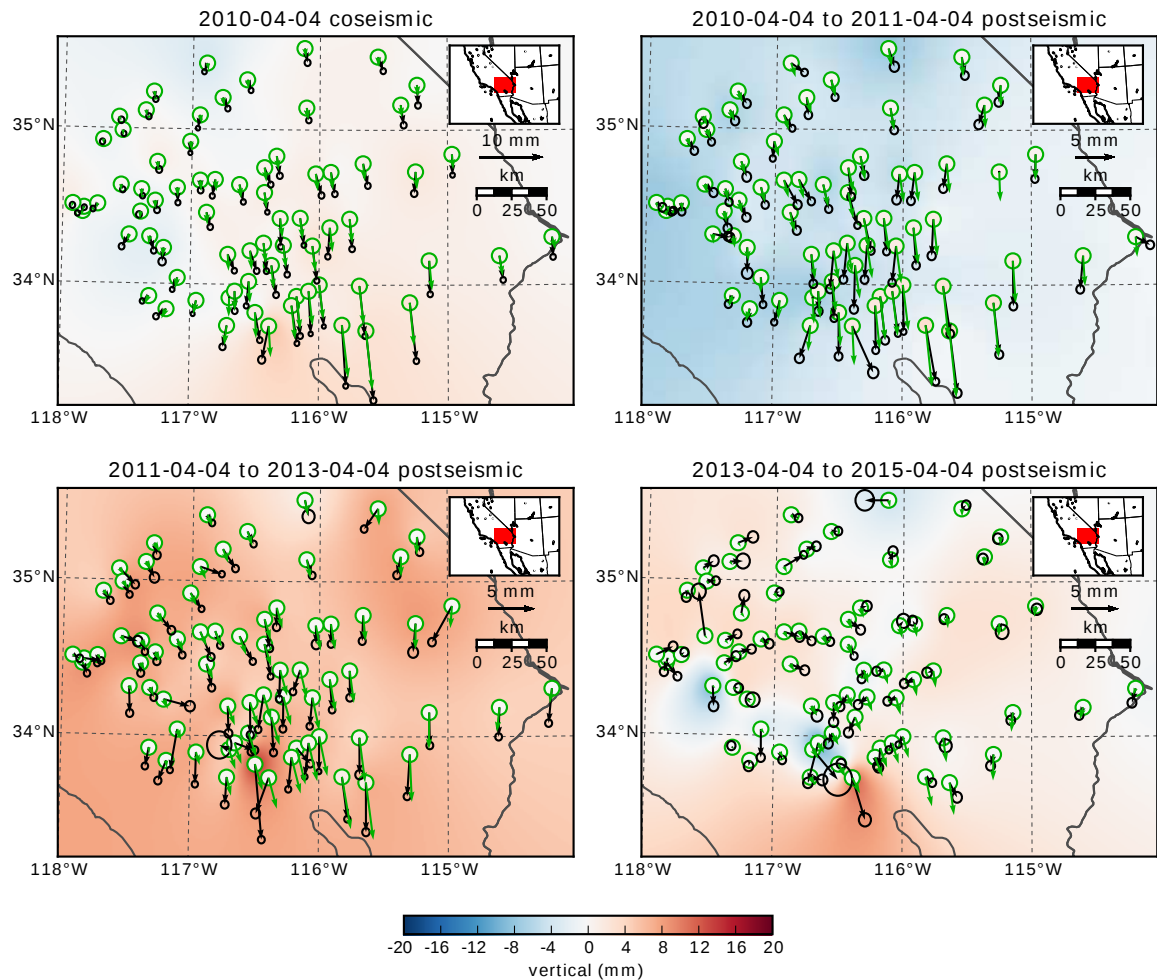


**Figure 5.** Same as Figure 4 but for far-field stations.

221

We estimate coseismic and time-dependent postseismic fault slip, both of which are assumed to occur on a fault geometry modified from *Wei et al.* [2011b]. Field studies [*Fletcher et al.*, 2014] and LIDAR observations [*Oskin et al.*, 2012] have revealed a significantly more complicated fault geometry than what was inferred by *Wei et al.* [2011b], especially within the Sierra Cucapah. However, we find that a relatively simple coseismic fault geometry based on [*Wei et al.*, 2011b] is adequate because most of the stations used in this study are sufficiently far from the El Mayor-Cucapah rupture zone that they are insensitive to the details in the fault geometry found by *Fletcher et al.* [2014] and *Oskin et al.* [2012]. The fault geometry used in this study (Figure 1) consists of the two main fault segments inferred by *Wei et al.* [2011b], where the northern segment runs through the Sierra Cucapah up to the US-Mexico border and the southern segment is the Indiviso fault which extends down to the Gulf of California. Both segments extend from the surface to 15 km depth. We extend the northern segment by 40 km to the north-west, motivated by the clustering of aftershocks on the northern tip of the coseismic rupture zone [*Hauksson et al.*, 2011; *Kroll et al.*, 2013]. This extended fault segment was also found to be necessary by *Rollins et al.* [2015] and *Pollitz et al.* [2012] in order to describe the postseismic deformation.

### 3.1 Elastic Postseismic Inversion

We consider a variety of rheologic models for the lower crust and upper mantle. The simplest rheologic model is to consider them to be effectively elastic and isotropic. In such case, the rheologic parameters consist of the Lamé parameters,  $\lambda$  and  $\mu$ , which are reasonably well known and we use the same values used by *Wei et al.* [2011b] throughout this paper (Table 1). The only unknown is the distribution of fault slip, which can be easily estimated from postseismic deformation through linear least squares. Using a subset of the GPS stations considered in this study, *Rollins et al.* [2015] found that three years of postseismic deformation following the El Mayor-Cucapah earthquake can be explained with afterslip on the coseismic fault plane without requiring any viscoelastic relaxation. We also perform an elastic slip inversion, but we use GPS stations within a larger radius about the El Mayor-Cucapah epicenter (400 km instead of  $\sim$ 200 km). Our forward problem describing predicted postseismic deformation  $u_{\text{pred}}$  in terms of time dependent fault slip,  $s$ , is

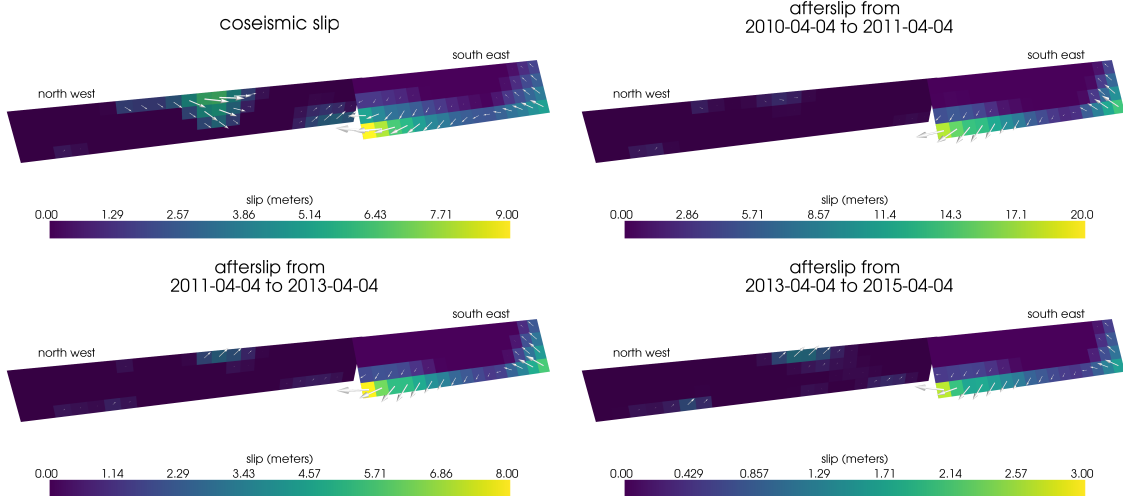
$$u_{\text{pred}}(x, t) = \int_F s(\xi, t) g(x, \xi) d\xi, \quad (9)$$

where  $F$  denotes the fault and  $g(x, \xi)$  is the elastic Green's function describing displacement at surface position  $x$  resulting from slip at  $\xi$  on the fault. We estimate coseismic slip and the rate of afterslip over the time intervals 0.0-0.125, 0.125-0.25, 0.5-1.0, 1.0-2.0, 2.0-3.0, 3.0-4.0, and 4.0-5.0 years after the earthquake. Each fault segment is discretized into roughly 4 km by 4 km patches and we estimate a strike-slip and dip component of slip for each patch. We impose that the direction of slip and slip rate are within  $45^\circ$  of right-lateral. We also add zeroth-order Tikhonov regularization so that our solution for  $s$  satisfies

$$\min_s \left( \left\| \frac{u_{\text{pred}}(s) - u_{\text{post}}}{\sigma_{\text{post}}} \right\|_2^2 + \lambda_s \|s\|_2^2 \right), \quad (10)$$

where  $\sigma_{\text{post}}$  is the uncertainty on postseismic displacements and  $\lambda_s$  is a penalty parameter which is chosen with a trade-off curve. We use Pylith [*Aagaard et al.*, 2013] to compute the Green's functions for this inversion as well as for the remaining inversions in this paper.

Our coseismic slip and afterslip solutions are shown in Figure 6. As with *Rollins et al.* [2015], we find that a large amount of afterslip on the southern fault segment is required to explain the observations. The potency of our inferred coseismic slip is  $3.2 \times 10^9 \text{ m}^3$ , equivalent to a Mw7.28 earthquake when assuming a shear modulus of 32 GPa. The potency of our inferred cumulative five years of afterslip is  $6.1 \times 10^9 \text{ m}^3$ , equivalent to a Mw7.46 earthquake, which is unrealistically large if we consider afterslip to be driven by coseismically induced



296 **Figure 6.** Coseismic slip and cumulative afterslip over the indicated intervals for the elastic model from  
297 Section 3.1. Color indicates the magnitude of slip while arrows indicate the motion of the hanging wall.

286 stresses. Figure 7 shows the time series for the observed and predicted postseismic displacements  
287 at stations along the El Mayor-Cucapah P axis. We show the radial component of displacements  
288 with respect to the El Mayor-Cucapah epicenter and we also rescale the displacements so that the  
289 difference between the minimum and maximum observed displacements are the same for each station.  
290 Our elastic slip model accurately describes near-field postseismic deformation and systematically  
291 underestimates postseismic deformation at epicentral distances  $\gtrsim 150$  km. When the fault segments used in  
292 the inversion are extended down to 30 km depth, rather than 15 km, the systematic far-field residuals are  
293 smaller but remain apparent. Because an elastic model requires an unrealistic amount of afterslip and is unable to predict far-field  
294 deformation, we move on to consider viscoelastic models in the next section.  
295

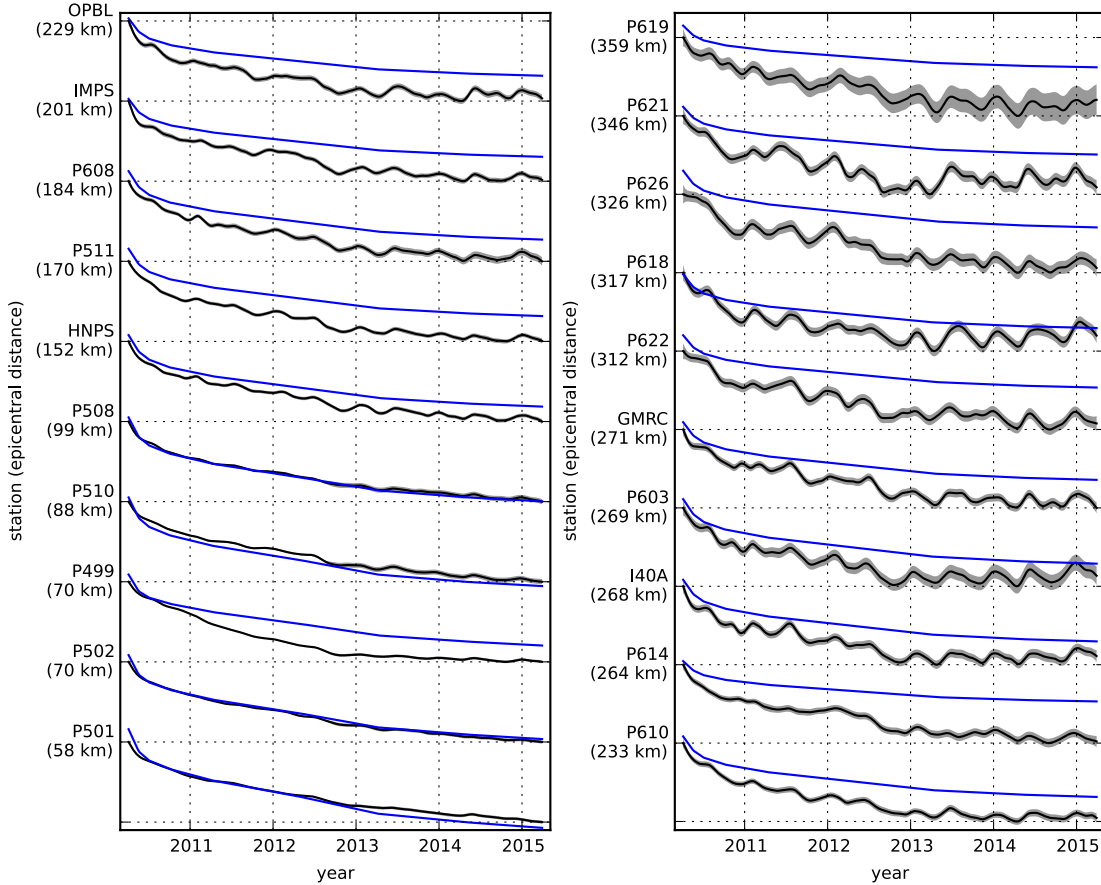
### 303 3.2 Early Postseismic Inversion

304 For any linear viscoelastic rheology of the crust and mantle, postseismic displacements  
305 resulting from time dependent fault slip can be described as

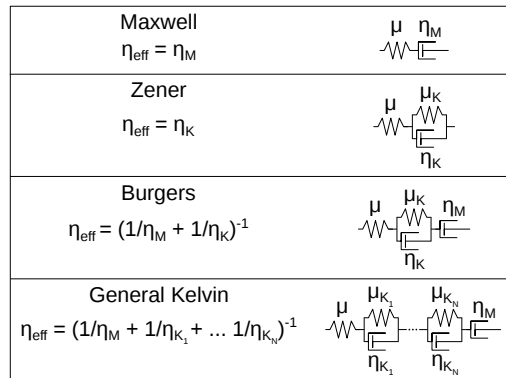
$$u_{\text{pred}}(x, t) = \int_F s(\xi, t) g(x, \xi) d\xi + \int_0^t \int_F s(\xi, \tau) f(t - \tau, x, \xi) d\xi d\tau, \quad (11)$$

306 where  $f(t, x, \xi)$  describes the time-dependent velocity at  $x$  resulting from viscoelastic relax-  
307 ation of stresses induced by slip at  $\xi$ .  $f$  is a function of  $\lambda$ ,  $\mu$ , and any additional rheologic pa-  
308 rameters controlling the viscoelastic response, which are generally not well known. Schematic  
309 representations of the viscoelastic rheologic models considered in this study are shown in Fig-  
310 ure 8. We discuss these rheologic models and their use in geophysical studies in Section 4.

313 In order to greatly simplify the inverse problem, we use the method described in *Hines*  
314 and *Hetland* [2016] to constrain an initial effective viscosity structure from the early postseis-  
315 mic deformation. Our method utilizes the fact that coseismic stresses throughout the crust and  
316 upper mantle depend on the instantaneous elastic parameters and are independent of the vis-  
317 coelastic parameters which we wish to estimate. Immediately following an earthquake, each  
318 parcel will have a strain rate that is proportional to the coseismic stress and inversely propor-  
319 tional to the parcel's effective viscosity,  $\eta_{\text{eff}}$ . Using one-dimensional viscoelastic models, we  
320 define the effective viscosity as



298 **Figure 7.** Scaled radial component of observed postseismic displacements  $u_{\text{obs}}$  (black) and displacements  
 299 predicted by the best fitting elastic model  $u_{\text{pred}}$  (blue). Downward motion indicates that the station is moving  
 300 toward the El Mayor-Cucapah epicenter. Displacement time series are scaled so that the minimum and maximum  
 301 observed values lie on the grid lines. The 68% confidence interval for the observed displacements are  
 302 shown in gray.



311 **Figure 8.** Schematic illustration of the rheologic models considered in this paper as well as their effective  
 312 viscosities.

$$\eta_{\text{eff}} = \frac{\sigma}{\dot{\varepsilon}} \Big|_{t=0}, \quad (12)$$

321 where  $\sigma$  is an applied stress at  $t = 0$  and  $\dot{\varepsilon}$  is the resulting strain rate. Figure 8 shows how  
 322  $\eta_{\text{eff}}$  relates to the parameters for various linear viscoelastic rheologies. We can deduce that the  
 323 initial rate of surface deformation resulting from viscoelastic relaxation is a summation of the  
 324 surface deformation resulting from relaxation in each parcel, scaled by the reciprocal of the  
 325 parcel's effective viscosity. That is to say

$$f(0, x, \xi) = \int_L \frac{h(x, \xi, \zeta)}{\eta_{\text{eff}}(\zeta)} d\zeta, \quad (13)$$

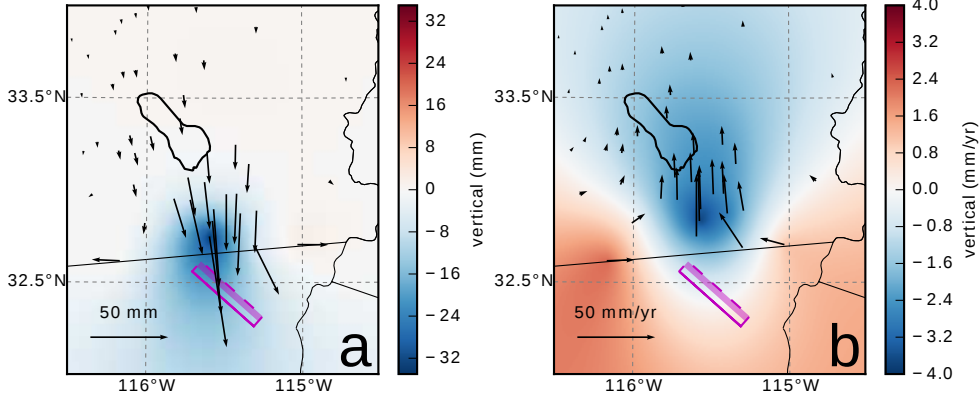
326 where  $L$  denotes the crust and mantle and  $h(x, \xi, \zeta)$  describes the initial rate of deformation  
 327 resulting from viscoelastic relaxation at  $\zeta$  induced by slip at  $\xi$ . We can combine eq. (13) with  
 328 eq. (11) to get a first order approximation for early postseismic deformation,

$$u_{\text{pred}}(x, t) \approx \int_F s(\xi, t) g(x, \xi) d\xi + \int_0^t \int_F \int_L \frac{s(\tau, \xi)}{\eta_{\text{eff}}(\zeta)} h(x, \xi, \zeta) d\xi d\zeta d\tau, \quad (14)$$

329 which is valid for as long as the rate of deformation resulting from viscoelastic relaxation is  
 330 approximately constant. Although eq. (14) may only be valid for a short portion of the post-  
 331 seismic period, its utility becomes apparent when noting that  $g$  and  $h$  are only functions of  
 332 the fault geometry and instantaneous elastic properties,  $\lambda$  and  $\mu$ , and thus  $g$  and  $h$  can be com-  
 333 puted numerically as a preprocessing step. The forward problem in eq. (14) can then be rapidly  
 334 evaluated for any realization of  $s$  and  $\eta_{\text{eff}}$ . This is in contrast to evaluating the full forward  
 335 problem, eq. (11), numerically for each realization of  $s$  and the unknown rheologic proper-  
 336 ties.

337 Details on how eq. (14) is used to estimate  $s$  and  $\eta_{\text{eff}}$  from postseismic deformation can  
 338 be found in *Hines and Hetland* [2016]. A non-linear Kalman filter based inverse method can  
 339 also be used to estimate  $s$  and  $\eta_{\text{eff}}$  in a manner akin to *Segall and Mathews* [1997] or *McGuire*  
 340 and *Segall* [2003], in which we would not have to explicitly impose a time dependent parametriza-  
 341 tion of  $s$ . We have thoroughly explored Kalman filter based approaches, but we ultimately pre-  
 342 fer the method described in *Hines and Hetland* [2016] because of its relative simplicity. More-  
 343 over, we believe the piecewise continuous representation of slip with respect to time to be suf-  
 344 ficiently general for the resolving power of these GPS data.

345 We estimate coseismic slip and afterslip with the same spatial and temporal discretiza-  
 346 tion as in Section 3.1. Simultaneously, we estimate  $\eta_{\text{eff}}$  within six vertically stratified layers  
 347 which have depths ranging from 15-30 km, 30-60 km, 60-90 km, 90-120 km, 120-150 km,  
 348 as well as from 150 km to the bottom of our numerical model domain at 800 km. We again  
 349 restrict fault slip to occur between 0 and 15 km depth, which is done in order to help elim-  
 350 inate inevitable non-uniqueness in the inversion. It has long been recognized that fault slip at  
 351 sufficiently great depths can produce surface deformation that is indistinguishable from vis-  
 352 coelastic relaxation, at least in two-dimensional earthquake models [Savage, 1990]. Addition-  
 353 ally, we note that when simultaneously estimating both afterslip and viscosity in the lower crust,  
 354 the inverse problem becomes particularly ill-posed. This ill-posedness is illustrated in Figure  
 355 9, which shows the displacements resulting from a meter of slip on a fault extending from 15  
 356 to 30 km depth and the initial velocity resulting from subsequent viscoelastic relaxation in the  
 357 lower crust, which is given a viscosity of  $10^{18}$  Pa s. In this demonstration, the viscoelastic re-  
 358 laxation is entirely driven by the fault slip in the lower crust. The horizontal displacements  
 359 from fault slip are in the opposite direction as the displacements resulting from viscoelastic  
 360 relaxation. This means that surface displacements resulting from afterslip at lower crustal depths  
 361 can be cancelled out, at least partially, by a low viscosity lower crust. We eliminate this null  
 362 space by allowing only one mechanism in the lower crust, which we choose to be viscoelas-  
 363 tic relaxation. This is not to say that we do not believe deep afterslip to be a possibility; rather,  
 364 we restrict slip to seismogenic depths as a modeling necessity. Although, it has been noted



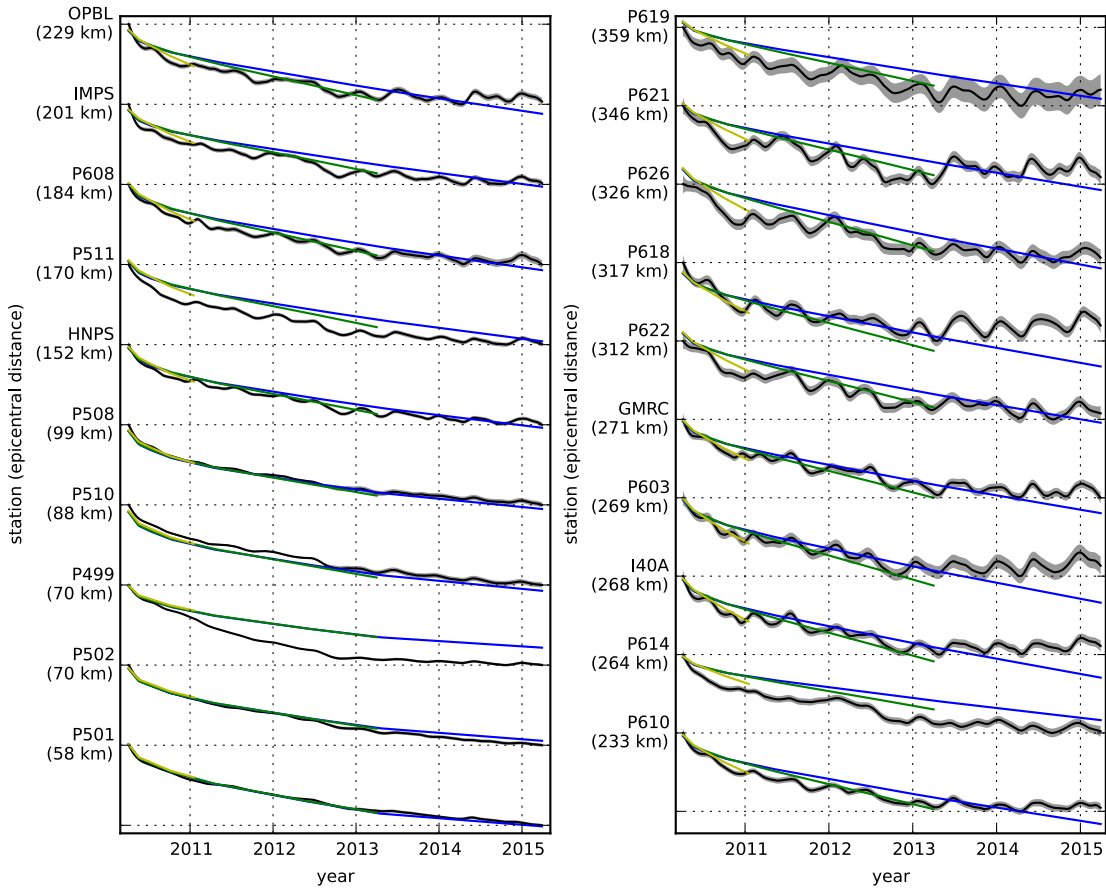
367 **Figure 9.** Displacements resulting from fault slip at lower crustal depths (a), and initial velocities resulting  
 368 from subsequent relaxation of a viscoelastic lower crust (b). The fault segment dips  $75^{\circ}$  to the north-east and  
 369 its surface projection is outlined in magenta. The highlighted area on the fault extends from 15 to 30 km depth  
 370 and indicates where 1 meter of right-lateral slip was imposed. The elastic properties of the crust and mantle  
 371 are the same as in Table 3, and  $\eta_{\text{eff}}$  is  $10^{18}$  Pa s in the lower crust. Vertical displacements are interpolated  
 372 between station locations.

365 that the pattern of vertical postseismic deformation following the El Mayor-Cucapah earthquake  
 366 indicates that a significant amount of afterslip must be shallow [Rollins *et al.*, 2015].

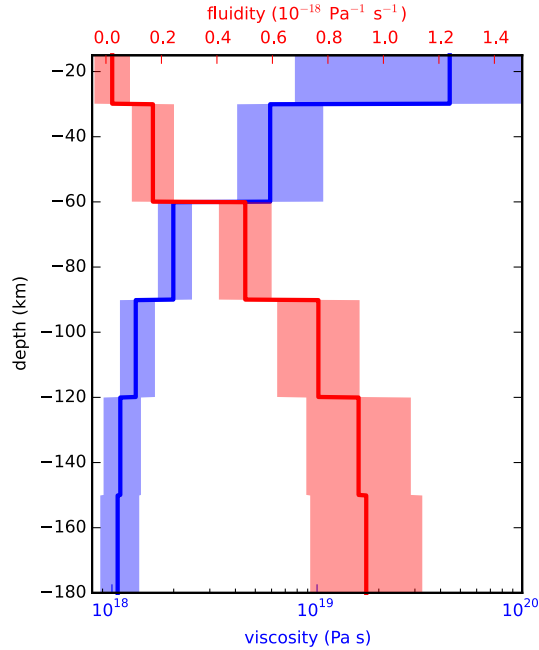
373 We must determine at which point the early postseismic approximation breaks down, which  
 374 we will denote as  $t_{\text{bd}}$ . As noted, eq. (14) is valid for approximately as long as the rate of de-  
 375 formation resulting from viscoelastic relaxation is approximately constant. We can almost cer-  
 376 tainly assume that deformation at the most far-field stations, which are  $\sim 400$  km away from  
 377 the El Mayor-Cucapah epicenter, is the result of viscoelastic relaxation. The approximation  
 378 should then be valid for as long as a linear trend adequately approximates the far-field de-  
 379 formation. Using this logic, it would appear that  $t_{\text{bd}}$  is about one year after the El Mayor-Cucapah  
 380 earthquake. Another way to determine  $t_{\text{bd}}$  is to find the best fitting prediction of eq. (14) to  
 381 observed deformation using increasing durations of the postseismic time series.  $t_{\text{bd}}$  should be  
 382 the point when eq. (14) is no longer capable of describing the observed deformation without  
 383 incurring systematic misfits. When using eq. (14) to fit the entire five years of postseismic dis-  
 384 placements, we see that the near-field displacements (e.g., station P501) are accurately pre-  
 385 dicted. When looking at displacements in the far-field (e.g., station P621), we see that eq. (14)  
 386 overestimates the rate of deformation in the later postseismic period and underestimates the  
 387 rate of deformation in the early period (Figure 10). Due to the low signal-to-noise ratios for  
 388 far-field stations, it is difficult to determine at what point eq. (14) is no longer able to predict  
 389 the observed displacements; however, we settle on  $t_{\text{bd}} = 0.8$  years after the earthquake, while  
 390 acknowledging that the choice is subjective. As noted in Hines and Hetland [2016], overes-  
 391 timating  $t_{\text{bd}}$  will result in a bias towards overestimating  $\eta_{\text{eff}}$ , while picking a  $t_{\text{bd}}$  which is too  
 392 low will not necessarily result in a biased estimate of  $\eta_{\text{eff}}$ , although the uncertainties would  
 393 be larger. We can then consider inferences of  $\eta_{\text{eff}}$  to be an upper bound on the viscosity needed  
 394 to describe the far-field rate of deformation during the first 0.8 years of postseismic deforma-  
 395 tion.

398 We estimate coseismic slip, afterslip, and effective viscosities by solving

$$\min_{s, \eta_{\text{eff}}} \left( \left\| \frac{u_{\text{pred}}(s, \eta_{\text{eff}}) - u_{\text{post}}}{\sigma_{\text{post}}} \right\|_2^2 + \lambda_s \|s\|_2^2 + \lambda_\eta \|\nabla \eta_{\text{eff}}^{-1}\|_2^2 \right), \quad (15)$$



396 **Figure 10.** Observed postseismic displacements (black) and best fitting predictions of eq. (14) to 5.0 (blue),  
 397 3.0 (green), and 0.8 (yellow) years of the postseismic data.

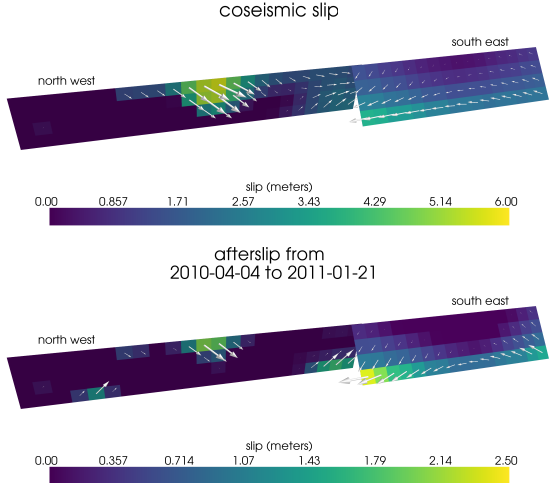


423 **Figure 11.** Effective viscosities and associated fluidities inferred by fitting eq. (14) to the first 0.8 years of  
 424 postseismic displacements. 95% confidence intervals, estimated from bootstrapping, are indicated by color  
 425 fields.

399 where  $u_{\text{post}}$  consists of the first 0.8 years of postseismic deformation and  $u_{\text{pred}}$  are the pre-  
 400 dicted displacements from eq. (14). Due to inherent non-uniqueness, we have added zeroth-  
 401 order Tikhonov regularization to estimates of  $s$  and second-order Tikhonov regularization to  
 402 estimates of effective fluidity  $\eta_{\text{eff}}^{-1}$ . The degree to which we impose the regularization on slip  
 403 and fluidity is controlled by the penalty parameters  $\lambda_s$  and  $\lambda_\eta$ , which are chosen with trade-  
 404 off curves. Our goal here is to get a prior constraint on  $\eta_{\text{eff}}$  to minimize the amount of search-  
 405 ing we have to do when describing the postseismic deformation over the full five years, which  
 406 we do in Section 3.3. Estimates of  $s$  made here will not be used in Section 3.3, and so the  
 407 motivation behind adding regularization to  $s$  is to ensure that the slip driving viscoelastic re-  
 408 laxation in eq. (14) is sensible.

409 Our estimated effective viscosities, and corresponding fluidities, are shown in Figure 11.  
 410 Although fluidity is rarely used in geophysical literature, eq. (13) is linear with respect to flu-  
 411 idity and so the fluidity indicates the amplitude of the viscoelastic signal coming from each  
 412 layer. We also show the 95% confidence intervals for estimated viscosities and fluidities but  
 413 we note that the uncertainties tend to be underestimated due to the added regularization [Aster  
 414 *et al.*, 2011]. A robust feature that we see is that the largest jump in fluidity is at 60 km depth,  
 415 which is consistent with the range of lithosphere-asthenosphere boundary depths inferred by  
 416 Lekic *et al.* [2011]. This transitional depth is also consistent with the the viscosity structure  
 417 required to explain far-field postseismic deformation following the Hector Mine earthquake  
 418 [Freed *et al.*, 2007]. We find that the viscosity below 60 km depth needs to be  $\sim 10^{18}$  Pa s to  
 419 describe the early rate of postseismic deformation at far-field stations while the lower crust  
 420 and uppermost mantle need to be relatively stronger. The viscosity of the lower crust is the  
 421 least well constrained as there is no evidence of relaxation in that layer, meaning that it is ef-  
 422 fectively elastic over the first 0.8 years after the earthquake.

426 Our initial estimate for coseismic slip and cumulative afterslip over the first 0.8 years  
 427 after the El Mayor-Cucapah earthquake are shown in Figure 12. Similar to our elastic slip model  
 428 from Section 3.1, a significant amount of right-lateral and normal coseismic slip is inferred



441 **Figure 12.** Coseismic slip and afterslip inferred by fitting eq. (14) to the first 0.8 years of postseismic  
442 displacements.

429 to be on the Sierra Cucapah fault segment. Our coseismic slip solution is consistent with field  
430 studies [Fletcher *et al.*, 2014] and the model from Wei *et al.* [2011b]. The potency of inferred  
431 coseismic slip is  $3.3 \times 10^9 \text{ m}^3$ , which is also about the same as that inferred from Section  
432 3.1. The present inference of afterslip on the Indiviso fault is significantly less than what was  
433 found in the Section 3.1 where we did not account for viscoelasticity. When fault slip is si-  
434 multaneously estimated with viscosity, the potency of inferred afterslip over the first 0.8 years  
435 after the earthquake is  $0.85 \times 10^9 \text{ m}^3$ , compared to  $3.5 \times 10^9 \text{ m}^3$  when we assume the crust  
436 and upper mantle are elastic. The significant amount of afterslip inferred on the Indiviso fault  
437 seems to be compensating for unmodeled viscoelastic relaxation at depths greater than 60 km.  
438 The fact that there is still an appreciable amount of afterslip inferred on the Indiviso fault raises  
439 the question of whether it is compensating for viscoelastic relaxation that is more localized  
440 than what we allow for since we only estimate depth dependent variations in viscosity.

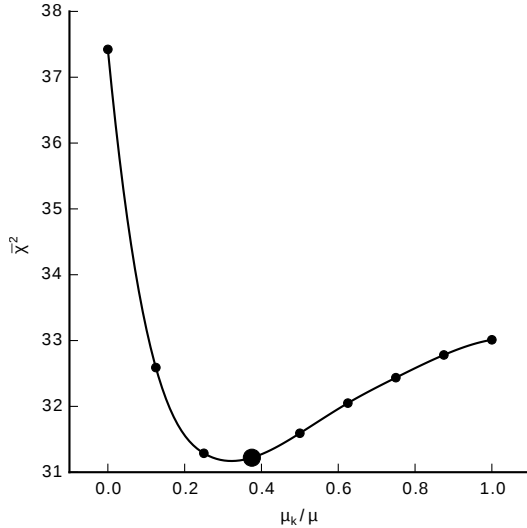
### 443 3.3 Full Postseismic Inversion

444 In the previous section, we used the inverse method from Hines and Hetland [2016] to  
445 constrain the effective viscosity structure required to explain the first 0.8 years of postseismic  
446 deformation. In this section, we use these effective viscosities as a prior constraint when search-  
447 ing for models which are capable of describing the available five years of postseismic data,  
448 where our forward problem is now eq. (11) rather than the approximation given by eq. (14).  
449 We perform a series of fault slip inversions assuming a variety of rheologies for the lower crust  
450 and upper mantle which are consistent with our findings from Section 3.2. We appraise each  
451 model using the mean chi-squared value,

$$\bar{\chi}^2 = \frac{1}{N} \left\| \frac{u_{\text{pred}} - u_{\text{obs}}}{\sigma_{\text{obs}}} \right\|_2^2, \quad (16)$$

452 where  $N$  is the number of observations.

453 We first assume that the crust and mantle can be described with a Maxwell rheology,  
454 and we set the steady-state viscosity  $\eta_M$  equal to our inference of  $\eta_{\text{eff}}$ . We compute  $f$  and  $g$   
455 from eq. (11) using Pylith, and we use the same spatial and temporal discretization of  $s$  as  
456 in Sections 3.1 and 3.2. We estimate  $s$  using linear least squares and find a misfit of  $\bar{\chi}^2 =$

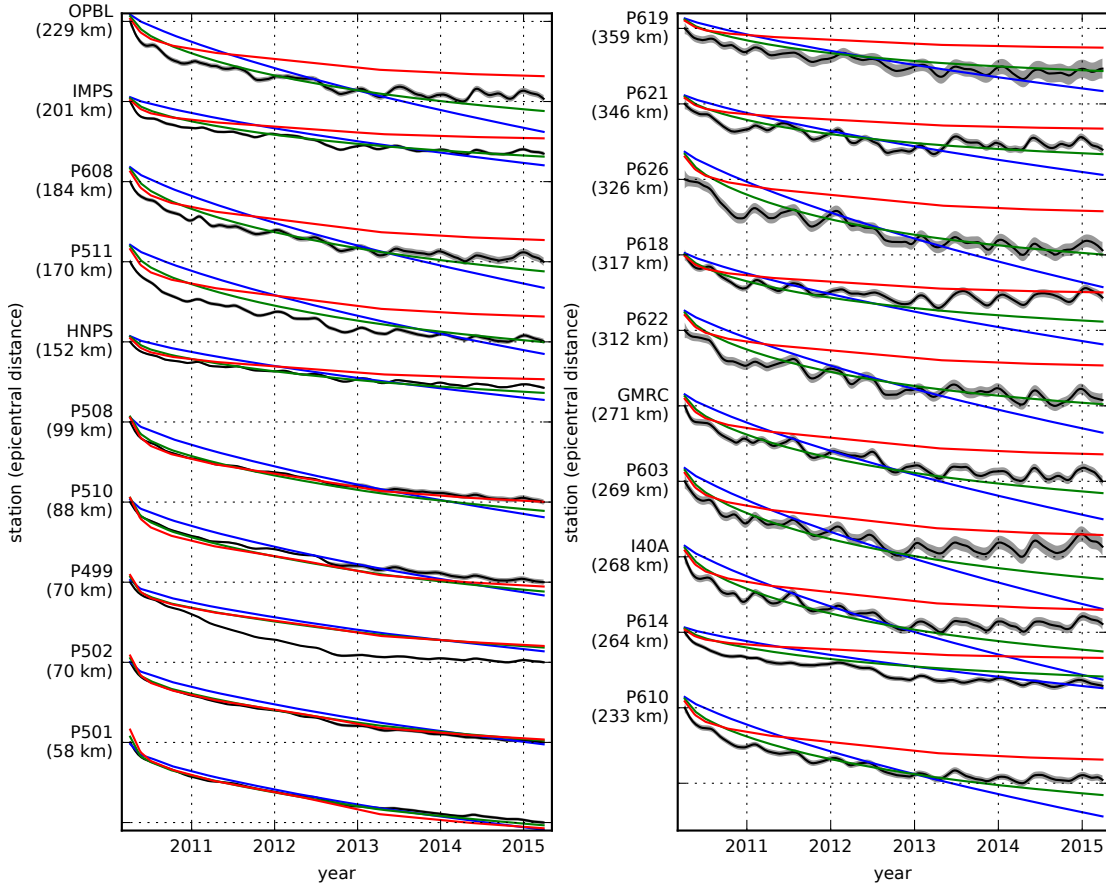


482 **Figure 13.** Mean chi-squared value for the best fitting slip model as a function of the transient shear modu-  
 483 lus relative to the elastic shear modulus in a Zener upper mantle. Large dot indicates our preferred ratio.

457 37.4. For comparison,  $\bar{\chi}^2 = 35.3$  for the elastic model from Section 3.1. The Maxwell vis-  
 458 coelastic model has a larger misfit because it tends to overestimate the rate of deformation af-  
 459 ter about three years (Figure 14). Since our initial estimates of  $\eta_{\text{eff}}$  may be biased towards over-  
 460 estimating viscosities, we have also performed the slip inversion where we use uniformly lower  
 461 viscosities in the crust and mantle. However, decreasing the viscosity only increases the mis-  
 462 fit. Although, the viscosities used here are consistent with the successful Maxwell viscoelas-  
 463 tic models found by *Rollins et al.* [2015] and *Spinler et al.* [2015], which had mantle viscosi-  
 464 ties on the order of  $10^{18}$  Pa s and relatively higher lower crustal viscosities, we find that such  
 465 a model is incapable of describing the entire postseismic time series. *Pollitz et al.* [2001] sim-  
 466 ilarly recognized this deficiency in a Maxwell rheology, which then motivated their exploration  
 467 of a Burgers rheology upper mantle [*Pollitz*, 2003].

468 Instead of exploring a Burgers rheology mantle, which introduces two new parameters  
 469 that need to be estimated, the transient viscosity  $\eta_K$  and transient shear modulus  $\mu_K$ , we first  
 470 consider a Zener rheology for the mantle, which only introduces one additional unknown pa-  
 471 rameter,  $\mu_K$ . We assume that the lower crust still has a Maxwell rheology. The steady-state  
 472 viscosity in the crust and the transient viscosity in the mantle are set equal to the inferred ef-  
 473 fective viscosities. We then estimate the ratio of shear moduli  $\frac{\mu_K}{\mu}$ . We compute nine differ-  
 474 ent sets of Green's functions,  $f$  and  $g$ , where we assume values of  $\frac{\mu_K}{\mu}$  ranging from 0 to 1.  
 475 The former being a degenerate case where the Zener model reduces to the above Maxwell model.  
 476 We estimate coseismic slip and afterslip for each realization of  $\frac{\mu_K}{\mu}$ . The shear moduli ratio  
 477 that yields the best prediction to the observed postseismic displacements is found to be 0.375  
 478 which produces a misfit of  $\bar{\chi}^2 = 31.2$  (Figure 13). The improvement in the Zener model over  
 479 the Maxwell model can be clearly seen in the fit to the far-field data (Figure 14). The Zener  
 480 model does a significantly better job at explaining the transient rate of far-field deformation  
 481 throughout the five years.

489 Because we are able to adequately describe the available five years of postseismic de-  
 490 formation with a Zener model, we do not find it necessary to explore the parameter space for  
 491 a more complicated Burgers rheology. However, since the Zener model is a Burgers model with  
 492 an infinite steady-state viscosity, we can conclude that any Burgers rheology that has a tran-  
 493 sient viscosity consistent with that found in Section 3.2 and a steady-state viscosity  $\gtrsim 10^{20}$



484  
485  
486  
487  
488 **Figure 14.** Observed postseismic displacements (black). Predicted postseismic displacements for the best  
fitting slip model when assuming a Maxwell viscoelastic lower crust and upper mantle (blue). Predicted post-  
seismic displacements for the best fitting slip model when assuming a Maxwell viscoelastic lower crust and a  
Zener viscoelastic upper mantle (green). The effective viscosities are the same for both models and are shown  
in Figure 11.

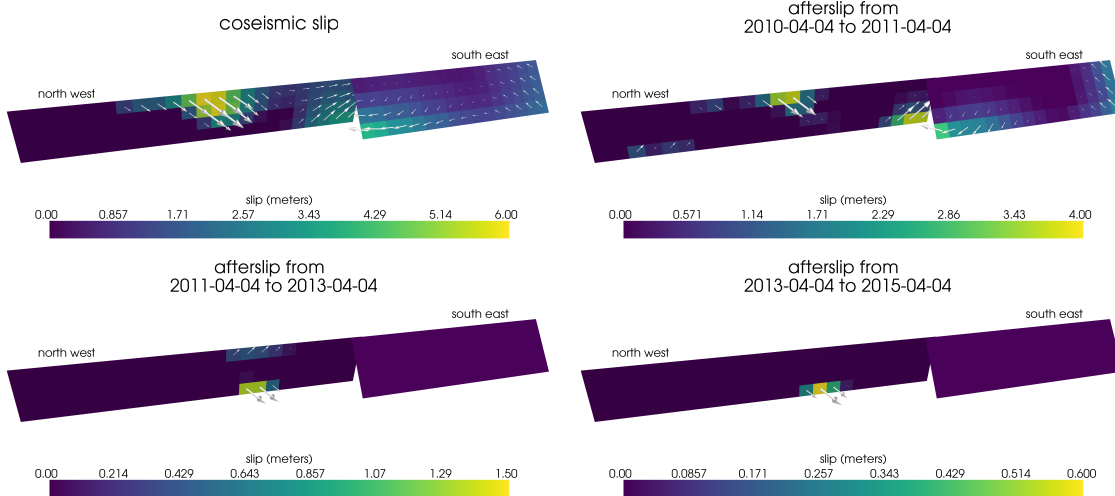
494 Pa s, which is effectively infinite on the time scale of five years, would also be able to sat-  
495 isfactorily describe the observable postseismic deformation.

496 The regularized inference of coseismic slip and afterslip for our preferred Zener model  
497 is shown in Figure 15. The inferred coseismic potency is  $3.0 \times 10^9$  m<sup>3</sup>, equivalent to a Mw7.26  
498 earthquake, and most of the slip is shallow and on the Sierra Cucapah fault segment. The po-  
499 tency of five years of afterslip is  $1.1 \times 10^9$  m<sup>3</sup>. Most of the afterslip in our preferred model  
500 occurs within the first year after the earthquake and coincides with the location of our inferred  
501 coseismic slip. Inferred afterslip within the first year is accounting for the most rapid near-  
502 field transient deformation. After one year, afterslip is inferred to be deeper down on the Sierra  
503 Cucapah segment, which is describing much of the sustained near-field postseismic deforma-  
504 tion. We emphasize, that the GPS station closest to where we infer afterslip, P496, is still about  
505 30 km away, which is too far for us to conclusively argue for sustained localized deformation  
506 rather than shallow distributed deformation. The deep afterslip inferred after one year could  
507 potentially be describing deformation resulting from lower crustal flow. To test this, we have  
508 modified our preferred model by decreasing the lower crustal viscosity from  $5.91 \times 10^{19}$  Pa  
509 s to  $1 \times 10^{19}$  Pa s, which is still consistent with our viscosity inference from Section 3.2, and  
510 inverted for fault slip. We find that a model with a weaker lower crust adequately describes  
511 the postseismic displacements without any afterslip after one year, while still requiring about  
512 the same amount of afterslip over the first year. We do believe that the early, shallow after-  
513 slip on the Sierra Cucapah segment is a robust feature in our preferred model, while we are  
514 not confident in our inference of later deep afterslip.

515 the postseismic displacements predicted by our preferred model are shown in Figures  
516 4, 5 and 14. Overall, the trends in the near-field and far-field transient deformation are accu-  
517 rately described. In particular, the trends in far-field deformation are much better described  
518 by our preferred Zener model than either an elastic model or a model with a Maxwell viscoelas-  
519 tic mantle (Figure 14). There are a few areas where we have notable misfit. Most of our mis-  
520 fit is for the near-field stations in the Imperial Valley, and we attribute this misfit to our rel-  
521 atively simple fault geometry, which does not account for potential fault slip in the Imperial  
522 Valley triggered by the El Mayor-Cucapah earthquake [Wei *et al.*, 2011a, 2015]. In particu-  
523 lar, we are unable to model the sustained, rapid rate of deformation at station P496, which sug-  
524 gests that this station could be influenced by a more localized deformation mechanism than  
525 is considered in this study. Additionally, we see systematic misfit in the later postseismic pe-  
526 riod west of the Landers and Hector Mine earthquakes, which may be the result of unmod-  
527 eled postseismic deformation resulting from those earthquakes. Lastly, there are clear discrep-  
528 ancies between the observed and predicted vertical deformation following the first year after  
529 the El Mayor Cucapah earthquake. We observe a broad uplift throughout Southern Califor-  
530 nia, which is inconsistent with any postseismic model.

## 534 4 Discussion

535 It has long been recognized that deep afterslip and viscoelastic relaxation following an  
536 upper crustal earthquake can result in similar horizontal ground deformation at the surface [e.g.  
537 Savage, 1990; Pollitz *et al.*, 2001; Hearn, 2003; Feigl and Thatcher, 2006]. The similarity of  
538 the horizontal postseismic deformation results in a non-uniqueness in inferences of afterslip  
539 or viscoelastic relaxation. In contrast, the spatial pattern of vertical postseismic deformation  
540 has been proposed to be a discriminant between deep afterslip and viscoelastic relaxation [e.g.  
541 Pollitz *et al.*, 2001; Hearn, 2003]. It is, however, important to note that patterns of vertical de-  
542 formation are very sensitive to the depth-dependence of viscosity below the upper crust [Yang  
543 and Toksöz, 1981; Hetland and Zhang, 2014]. The similarity between deformation resulting  
544 from deep afterslip and viscoelastic relaxation of coseismic stresses is different from the ill-  
545 posedness described in Section 3.2. In our method, any inferred afterslip will also mechani-  
546 cally drive additional viscoelastic relaxation. The horizontal deformation resulting from deep  
547 afterslip will generally be in the opposite direction as horizontal deformation resulting from  
548 viscoelastic relaxation of subsequent stresses in the lower crust (Figure 9). As a result, there



531 **Figure 15.** Inferred coseismic slip and afterslip when assuming a Maxwell rheology in the lower crust and  
 532 a Zener rheology in the upper mantle. The transient viscosity  $\eta_K$  in the mantle and steady-state viscosity  $\eta_M$   
 533 in the crust are set equal to the effective viscosities from Figure 11. We set  $\frac{\mu_K}{\mu} = 0.375$  in the upper mantle.

549 is a trade-off between inferences of deep afterslip and lower crustal viscosity. In our synthetic  
 550 tests in *Hines and Hetland* [2016], we have found that inverting surface deformation for af-  
 551 terslip and viscosity within the same depth interval tends to result in overestimated afterslip  
 552 and an underestimated viscosity.

553 Most postseismic studies assume Maxwell viscoelasticity in the lower crust and upper  
 554 mantle [e.g. *Nur and Mavko*, 1974; *Pollitz et al.*, 2000; *Hetland*, 2003; *Freed et al.*, 2006; *John-*  
 555 *son et al.*, 2009; *Hearn et al.*, 2009], which is the simplest viscoelastic rheologic model. In South-  
 556 ern California, postseismic studies following the Landers [*Pollitz et al.*, 2000], Hector Mine  
 557 [*Pollitz et al.*, 2001], and El Mayor-Cucapah earthquake [*Spinler et al.*, 2015; *Rollins et al.*, 2015],  
 558 have assumed Maxwell viscoelasticity in the lower crust and upper mantle and have inferred  
 559 upper mantle viscosities on the order of  $10^{17}$  to  $10^{18}$  Pa s and lower crust viscosities  $\gtrsim 10^{19}$   
 560 Pa s. These postseismic studies are consistent with *Kaufmann and Amelung* [2000] and *Cava-*  
 561 *lié et al.* [2007], who found that an upper mantle viscosity of  $10^{18}$  Pa s and a crustal viscos-  
 562 ity  $\gtrsim 10^{20}$  Pa s are necessary to describe subsidence resulting from changes in loading from  
 563 Lake Mead. This isostatic adjustment is a process with similar spatial and temporal scales as  
 564 postseismic deformation, and thus the inferred viscosities of these two types of studies would  
 565 likely agree. While these studies found viscosities that are consistent with our effective vis-  
 566 cosities from Section 3.2, they are inconsistent with viscosity estimates made from geophys-  
 567 ical processes that occur over longer time scales. For example, *Lundgren et al.* [2009] found  
 568 that lower crust and upper mantle viscosities on the order of  $10^{21}$  and  $10^{19}$  Pa s, respectively,  
 569 are needed to describe interseismic deformation along the Southern San Andreas fault zone  
 570 in the Salton Sea region. An even higher mantle viscosity, on the order of  $10^{20}$  Pa s, is re-  
 571 quired to describe isostatic adjustment resulting from the draining of Lake Bonneville, which  
 572 occurs on the time scales of  $10^4$  years [*Crittenden*, 1967; *Bills and May*, 1987].

573 An additional deficiency with the Maxwell rheology is that it predicts a steady decay  
 574 in the rate of postseismic deformation over time, which fails to describe the commonly ob-  
 575 served rapid, early transience followed by a relatively steady rate of postseismic deformation.  
 576 One could explain the early transient postseismic deformation with fault creep and the later  
 577 phase with relaxation in a Maxwell viscoelastic lower crust and upper mantle [e.g. *Hearn et al.*,  
 578 *Johnson et al.*, 2009]. However, postseismic deformation at distances greater than  $\sim 200$

579 km from the El Mayor-Cucapah epicenter can only be attributed to viscoelastic relaxation [Freed  
 580 *et al.*, 2007] and we have demonstrated that the far-field deformation cannot be explained with  
 581 a Maxwell rheology (Figure 14).

582 We found that a Zener rheology in the upper mantle with a transient viscosity of  $\sim 10^{18}$   
 583 Pa s does a noticeably better job at predicting far-field postseismic deformation. A general-  
 584 ization of the Zener viscoelastic model, schematically represented as several Kelvin elements  
 585 connected in series, is commonly used to describe seismic attenuation [Liu *et al.*, 1976]. The  
 586 highest viscosity needed to describe seismic attenuation is on the order of  $10^{16}$  Pa s [Yuen and  
 587 Peltier, 1982] which has a characteristic relaxation time on the order of days. Even though  
 588 our inferred transient viscosity is orders of magnitude larger than that required for seismic at-  
 589 tenuation models, the two models are not incompatible. Rather, the delayed elasticity in seis-  
 590 mic attenuation models occurs on such short time scales that it can be considered part of the  
 591 instantaneous elastic phase of deformation associated with the preferred Zener model in this  
 592 study.

593 Of course, it has long been recognized that a Zener rheology provides an incomplete de-  
 594 scriptions of the asthenosphere, as it does not have the fluid-like behavior required to explain  
 595 isostatic rebound or convection in the mantle [O'Connell, 1971]. Yuen and Peltier [1982] pro-  
 596 posed a Burgers rheology with a low transient viscosity ( $\eta_K \approx 10^{16}$  Pa s) and high steady-  
 597 state viscosity ( $\eta_M \approx 10^{21}$  Pa s) to describe both seismic attenuation and long term geologic  
 598 processes. The justification of a Burger's rheology mantle is further supported by laboratory  
 599 experiments on olivine [Chopra, 1997]. Pollitz [2003] sought to describe postseismic defor-  
 600 mation following Hector Mine with a Burgers rheology mantle and they found a best fitting  
 601 transient viscosity of  $1.6 \times 10^{17}$  Pa s and steady-state viscosity of  $4.6 \times 10^{18}$  Pa s. While  
 602 the Burgers rheology was introduced as a means of bridging the gap between relaxation ob-  
 603 served in long and short term geophysical processes, the inferred steady state viscosity from  
 604 Pollitz [2003] is still inconsistent with the Maxwell viscosities inferred from studies on the earth-  
 605 quake cycle and Lake Bonneville. The transient viscosity inferred by Pollitz [2003] is constrained  
 606 by the earliest phase of postseismic deformation following the Hector Mine earthquake. While  
 607 Pollitz [2003] ruled out deep afterslip as an alternative mechanism based on inconsistent ver-  
 608 tical deformation, it is still possible to successfully describe all components of early postseis-  
 609 mic deformation following the Hector Mine earthquake with afterslip at seismogenic depths  
 610 [Jacobs *et al.*, 2002]. It is then possible that the preferred rheologic model from Pollitz [2003]  
 611 was biased towards inferring a particularly low transient viscosity by neglecting to account for  
 612 afterslip. This is in contrast to the present study, where we have inferred a viscosity structure  
 613 simultaneously with afterslip. We also argue that a transient rheology is necessary to explain  
 614 postseismic deformation; however, our preferred transient viscosity of  $\sim 10^{18}$  Pa s in the up-  
 615 per mantle is an order of magnitude larger than the transient viscosity found by Pollitz [2003].  
 616 Since a Zener model is able to describe the available postseismic deformation following the  
 617 El Mayor-Cucapah earthquake, any Burgers rheology with a steady-state viscosity that is  $\gtrsim$   
 618  $10^{20}$  Pa s, effectively infinite over five years, would also be able to describe the postseismic  
 619 deformation. Such a Burgers model might then be consistent with the steady-state viscosities  
 620 necessary for lake loading, interseismic deformation, and mantle dynamics.

## 621 5 Conclusion

622 We have extracted a filtered and smoothed estimate of postseismic deformation follow-  
 623 ing the El Mayor-Cucapah earthquake from GPS displacement time series. Our estimated post-  
 624 seismic deformation reveals far-field (epicentral distances beyond  $\sim 200$  km) transient defor-  
 625 mation which is largely undetectable after about three years. Near-field deformation exhibits  
 626 transience that decays to a sustained, elevated rate after about one or two years. We found that  
 627 near-field transient deformation can be explained with shallow afterslip, and the sustained rate  
 628 of near-field deformation can either be explained with continued afterslip or viscoelastic re-  
 629 laxation in the lower crust. Far-field transient deformation can be more definitively ascribed  
 630 to viscoelastic relaxation at depths greater than  $\sim 60$  km. Beneath that depth, a transient vis-

cosity of  $\sim 10^{18}$  Pa s is required to describe the rate of far-field deformation throughout the five years considered in this study. By describing the available postseismic deformation with a transient rheology in the mantle, our preferred model does not conflict with the generally higher steady-state viscosities inferred from geophysical processes occurring over longer time scales.

## 636 Acknowledgements

637 We thank Andy Freed for an illuminating discussion on the data used in this study. This  
 638 material is based on EarthScope Plate Boundary Observatory data services provided by UN-  
 639 AVCO through the GAGE Facility with support from the National Science Foundation (NSF)  
 640 and National Aeronautics and Space Administration (NASA) under NSF Cooperative Agree-  
 641 ment No. EAR-1261833. The data used in this study can be found at [www.unavco.org](http://www.unavco.org). This  
 642 material is based upon work supported by the National Science Foundation under Grant Num-  
 643 bers EAR 1045372 and EAR 1245263.

## 644 References

- 645 Aagaard, B. T., M. G. Knepley, and C. A. Williams (2013). A domain decomposition  
 646 approach to implementing fault slip in finite-element models of quasi-static and dy-  
 647 namic crustal deformation, *Journal of Geophysical Research: Solid Earth*, 118, doi:  
 648 10.1002/jgrb.50217.
- 649 Argus, D. F., M. B. Heflin, G. Peltzer, F. Crampé, and F. H. Webb (2005), Interseismic  
 650 strain accumulation and anthropogenic motion in metropolitan Los Angeles, *Journal of*  
 651 *Geophysical Research: Solid Earth*, 110(4), 1–26, doi:10.1029/2003JB002934.
- 652 Aster, R. C., B. Borchers, and C. H. Thurber (2011), Parameter Estimation and Inverse  
 653 Problems, vol. 90, Academic Press.
- 654 Bawden, G. W., W. Thatcher, R. S. Stein, K. W. Hudnut, and G. Peltzer (2001), Tectonic  
 655 contraction across Los Angeles after removal of groundwater pumping effects., *Nature*,  
 656 412(August), 812–815, doi:10.1038/35090558.
- 657 Bills, B. G., and G. M. May (1987), Lake Bonneville: Constraints on Lithospheric Thick-  
 658 ness and Upper Mantle Viscosity From Isostatic Warping of Bonneville, Provo, and  
 659 Gilbert Stage Shorelines, *Journal of Geophysical Research-Solid Earth and Planets*,  
 660 92(B11), 11,493–11,508, doi:10.1029/JB092iB11p11493.
- 661 Çakir, Z., S. Ergintav, H. Özener, U. Dogan, A. M. Akoglu, M. Meghraoui, and  
 662 R. Reilinger (2012), Onset of aseismic creep on major strike-slip faults, *Geology*,  
 663 40(12), 1115–1118, doi:10.1130/G33522.1.
- 664 Cavalié, O., M. P. Doin, C. Lasserre, and P. Briole (2007), Ground motion measurement in  
 665 the Lake Mead area, Nevada, by differential synthetic aperture radar interferometry time  
 666 series analysis: Probing the lithosphere rheological structure, *Journal of Geophysical*  
 667 *Research: Solid Earth*, 112(3), 1–18, doi:10.1029/2006JB004344.
- 668 Cetin, E., Z. Çakir, M. Meghraoui, S. Ergintav, and A. M. Akoglu (2014), Extent and  
 669 distribution of aseismic slip on the İsmetpaşa segment of the North Anatolian Fault  
 670 (Turkey) from Persistent Scatterer InSAR, *Geochemistry, Geophysics, Geosystems*, 15,  
 671 doi:10.1002/2014GC005307. Received.
- 672 Chopra, P. N. (1997), High-temperature transient creep in olivine rocks, *Tectonophysics*,  
 673 279, 93–111, doi:10.1016/S0040-1951(97)00134-0.
- 674 Crittenden, M. (1967), Viscosity and Finite Strength of the Mantle as Determined from  
 675 Water and Ice Loads\*, *Geophysical Journal of the Royal Astronomical ...*, pp. 261–279,  
 676 doi:10.1111/j.1365-246X.1967.tb06243.x.
- 677 Davis, J. L., B. P. Wernicke, and M. E. Tamisiea (2012), On seasonal signals in geode-  
 678 tic time series, *Journal of Geophysical Research: Solid Earth*, 117(1), 1–10, doi:  
 679 10.1029/2011JB008690.

- 680 Feigl, K. L., and W. Thatcher (2006), Geodetic observations of post-seismic transients in  
 681 the context of the earthquake deformation cycle, *Comptes Rendus - Geoscience*, **338**,  
 682 1012–1028, doi:10.1016/j.crte.2006.06.006.
- 683 Fletcher, J. M., O. J. Teran, T. K. Rockwell, M. E. Oskin, K. W. Hudnut, K. J. Mueller,  
 684 R. M. Spelz, S. O. Akciz, E. Masana, G. Faneros, E. J. Fielding, S. Leprince, A. E.  
 685 Morelan, J. Stock, D. K. Lynch, A. J. Elliott, P. Gold, J. Liu-Zeng, A. González-  
 686 Ortega, A. Hinojosa-Corona, and J. González-García (2014), Assembly of a large  
 687 earthquake from a complex fault system: Surface rupture kinematics of the 4 April  
 688 2010 El Mayor-Cucapah (Mexico) Mw 7.2 earthquake, *Geosphere*, **10**(4), 797–827,  
 689 doi:10.1130/GES00933.1.
- 690 Freed, A. M., R. Bürgmann, E. Calais, J. Freymueller, and S. Hreinsdóttir (2006), Impli-  
 691 cations of deformation following the 2002 Denali, Alaska, earthquake for postseismic  
 692 relaxation processes and lithospheric rheology, *Journal of Geophysical Research: Solid  
 693 Earth*, **111**, 1–23, doi:10.1029/2005JB003894.
- 694 Freed, A. M., R. Bürgmann, and T. Herring (2007), Far-reaching transient motions after  
 695 Mojave earthquakes require broad mantle flow beneath a strong crust, *Geophysical  
 696 Research Letters*, **34**, 1–5, doi:10.1029/2007GL030959.
- 697 Gonzalez-Ortega, A., Y. Fialko, D. Sandwell, F. A. Nava-pichardo, J. Fletcher,  
 698 J. Gonzalez-garcia, B. Lipovsky, M. Floyd, and G. Funning (2014), El Mayor-  
 699 Cucapah (Mw7.2) earthquake: early near-field postseismic deformation from In-  
 700 Sar and GPS observations, *Journal of Geophysical Research*, **119**, 1482–1497, doi:  
 701 10.1002/2013JB010193.Received.
- 702 Hauksson, E., J. Stock, K. Hutton, W. Yang, J. A. Vidal-Villegas, and H. Kanamori  
 703 (2011), The 2010 Mw 7.2 El mayor-cucapah earthquake sequence, Baja Califor-  
 704 nia, Mexico and Southernmost California, USA: Active seismotectonics along the  
 705 Mexican pacific margin, *Pure and Applied Geophysics*, **168**(3918), 1255–1277, doi:  
 706 10.1007/s00024-010-0209-7.
- 707 Hearn, E. H. (2003), What can GPS data tell us about the dynamics of post-seismic defor-  
 708 mation ?, (2003), 753–777.
- 709 Hearn, E. H., S. McClusky, S. Ergintav, and R. E. Reilinger (2009), Izmit earthquake post-  
 710 seismic deformation and dynamics of the North Anatolian Fault Zone, *Journal of Geo-  
 711 physical Research: Solid Earth*, **114**(August 2008), 1–21, doi:10.1029/2008JB006026.
- 712 Hetland, E. A. (2003), Postseismic relaxation across the Central Nevada Seismic Belt,  
 713 *Journal of Geophysical Research*, **108**(Figure 2), 1–13, doi:10.1029/2002JB002257.
- 714 Hetland, E. A., and G. Zhang (2014), Effect of shear zones on post-seismic deformation  
 715 with application to the 1997 Mw 7.6 manyi earthquake, *Geophysical Journal Interna-  
 716 tional*, **198**, 259–269, doi:10.1093/gji/ggu127.
- 717 Hines, T. T., and E. A. Hetland (2013), Bias in estimates of lithosphere viscosity from  
 718 interseismic deformation, *Geophysical Research Letters*, **40**(16), 4260–4265, doi:  
 719 10.1002/grl.50839.
- 720 Hines, T. T., and E. A. Hetland (2016), Rapid and simultaneous estimation of fault slip  
 721 and heterogeneous lithospheric viscosity from post-seismic deformation, *Geophysical  
 722 Journal International*, **204**(1), 569–582, doi:10.1093/gji/ggv477.
- 723 Jacobs, A., D. Sandwell, Y. Fialko, and L. Sichoux (2002), The 1999 (Mw7.1) Hector  
 724 Mine, California, Earthquake: Near-Field Postseismic Deformation from ERS Interfer-  
 725 ometry, *Bulletin of the Seismological Society of America*, **92**(May), 1433–1442.
- 726 Johnson, K. M., and P. Segall (2004), Viscoelastic earthquake cycle models with deep  
 727 stress-driven creep along the San Andreas fault system, *Journal of Geophysical Research  
 728 B: Solid Earth*, **109**, 1–19, doi:10.1029/2004JB003096.
- 729 Johnson, K. M., R. Bürgmann, and J. T. Freymueller (2009), Coupled afterslip and vis-  
 730 coelastic flow following the 2002 Denali Fault, Alaska earthquake, *Geophysical Journal  
 731 International*, **176**(3), 670–682, doi:10.1111/j.1365-246X.2008.04029.x.
- 732 Jónsson, S., P. Segall, R. Pedersen, and G. Bjornsson (2003), Post-earthquake ground  
 733 movements correlated to pore-pressure transients, *Nature*, **424**(July), 179–183, doi:

- 734                   10.1038/nature01758.1.
- 735     Kaufmann, G., and F. Amelung (2000), Reservoir-induced deformation and continental  
736       rheology in vicinity of Lake Mead, Nevada, *Journal of Geophysical Research*, 105(B7),  
737       16,341, doi:10.1029/2000JB900079.
- 738     Kroll, K. A., E. S. Cochran, K. B. Richards-Dinger, and D. F. Sumy (2013), Aftershocks  
739       of the 2010 Mw 7.2 El Mayor-Cucapah earthquake reveal complex faulting in the Yuha  
740       Desert, California, *Journal of Geophysical Research: Solid Earth*, 118(October), 6146–  
741       6164, doi:10.1002/2013JB010529.
- 742     Lekic, V., S. W. French, and K. M. Fischer (2011), Lithospheric Thinning Beneath Rifted  
743       Regions of Southern California, *Science*, 334(November), 783–787.
- 744     Liu, H.-P., D. L. Anderson, and H. Kanamori (1976), Velocity dispersion due to anelasticity;  
745       implications for seismology and mantle composition, *Geophysical Journal International*,  
746       47(1), 41–58, doi:10.1111/j.1365-246X.1976.tb01261.x.
- 747     Lundgren, P., E. A. Hetland, Z. Liu, and E. J. Fielding (2009), Southern San Andreas-San  
748       Jacinto fault system slip rates estimated from earthquake cycle models constrained by  
749       GPS and interferometric synthetic aperture radar observations, *Journal of Geophysical  
750       Research: Solid Earth*, 114(2), 1–18, doi:10.1029/2008JB005996.
- 751     McGuire, J. J., and P. Segall (2003), Imaging of aseismic fault slip transients recorded  
752       by dense geodetic networks, *Geophysical Journal International*, 155(3), 778–788, doi:  
753       10.1111/j.1365-246X.2003.02022.x.
- 754     Meade, B. J., and B. H. Hager (2005), Block models of crustal motion in southern Cal-  
755       ifornia constrained by GPS measurements, *Journal of Geophysical Research B: Solid  
756       Earth*, 110, 1–19, doi:10.1029/2004JB003209.
- 757     Murray, J. R., and P. Segall (2005), Spatiotemporal evolution of a transient slip event on  
758       the San Andreas fault near Parkfield, California, *Journal of Geophysical Research : Solid  
759       Earth*, 110(9), 1–12, doi:10.1029/2005JB003651.
- 760     Nur, A., and G. Mavko (1974), Postseismic viscoelastic rebound, *Science*, 183(4121),  
761       204–206, doi:10.1038/098448b0.
- 762     O'Connell, R. J. (1971), Rheology of the Mantle, *EOS, Transactions, American Geophys-  
763       ical Union*, 52, 140–142.
- 764     Osokin, M. E., J. R. Arrowsmith, A. Hinojosa Corona, A. J. Elliott, J. M. Fletcher, E. J.  
765       Fielding, P. O. Gold, J. J. Gonzalez Garcia, K. W. Hudnut, J. Liu-Zeng, and O. J. Teran  
766       (2012), Near-field deformation from the El Mayor-Cucapah earthquake revealed by  
767       differential LIDAR, *Science*, 335(6069), 702–705, doi:10.1126/science.1213778.
- 768     Pollitz, F., C. Wicks, and W. Thatcher (2001), Mantle Flow Beneath a Continental Strike-  
769       Slip Fault : Postseismic Deformation After the 1999 Hector Mine Earthquake, *Science*,  
770       1814(2001), 1814–1818, doi:10.1126/science.1061361.
- 771     Pollitz, F. F. (2003), Transient rheology of the uppermost mantle beneath the Mo-  
772       jave Desert, California, *Earth and Planetary Science Letters*, 215, 89–104, doi:  
773       10.1016/S0012-821X(03)00432-1.
- 774     Pollitz, F. F., G. Peltzer, and R. Bürgmann (2000), Mobility of continental mantle: Evi-  
775       dence from postseismic geodetic observations following the 1992 Landers earthquake,  
776       *Journal of Geophysical Research*, 105(1999), 8035, doi:10.1029/1999JB900380.
- 777     Pollitz, F. F., R. Bürgmann, and W. Thatcher (2012), Illumination of rheological mantle  
778       heterogeneity by the M7.2 2010 El Mayor-Cucapah earthquake, *Geochemistry, Geo-  
779       physics, Geosystems*, 13(6), 1–17, doi:10.1029/2012GC004139.
- 780     Rauch, H. E., F. Tung, and C. T. Striebel (1965), Maximum likelihood estimates of linear  
781       dynamic systems, *AIAA Journal*, 3(8), 1445–1450.
- 782     Riva, R. E. M., and R. Govers (2009), Relating viscosities from postseismic relaxation to  
783       a realistic viscosity structure for the lithosphere, *Geophysical Journal International*, 176,  
784       614–624, doi:10.1111/j.1365-246X.2008.04004.x.
- 785     Rollins, C., S. Barbot, and J.-P. Avouac (2015), Postseismic Deformation Following the  
786       2010 M7.2 El Mayor-Cucapah Earthquake : Observations , Kinematic Inversions , and  
787       Dynamic Models, *Pure and Applied Geophysics*, doi:10.1007/s00024-014-1005-6.

- 788 Savage, J. C. (1990), Equivalent strike-slip earthquake cycles in half-space and  
789 lithosphere-asthenosphere earth models, *Journal of Geophysical Research*, 95, 4873,  
790 doi:10.1029/JB095iB04p04873.
- 791 Savage, J. C., and J. L. Svart (2009), Postseismic relaxation following the 1992 M 7.3  
792 Landers and 1999 M 7.1 Hector Mine earthquakes , southern California, *Journal of*  
793 *Geophysical Research*, 114(B01401), doi:10.1029/2008JB005938.
- 794 Savage, J. C., J. L. Svart, and S. B. Yu (2005), Postseismic relaxation and transient creep,  
795 *Journal of Geophysical Research: Solid Earth*, 110, 1–14, doi:10.1029/2005JB003687.
- 796 Segall, P., and M. Mathews (1997), Time dependent inversion of geodetic data, *Journal of*  
797 *Geophysical Research*, 102.
- 798 Spinler, J. C., R. A. Bennett, C. Walls, L. Shawn, and J. J. G. Garcia (2015), As-  
799 sessing long-term postseismic deformation following the M7.2 4 April 2010, El  
800 Mayor-Cucapah earthquake with implications for lithospheric rheology in the  
801 Salton Trough, *Journal of Geophysical Research: Solid Earth*, 120, 3664–3679, doi:  
802 10.1002/2014JB011613.Received.
- 803 Wei, M., D. Sandwell, Y. Fialko, and R. Bilham (2011a), Slip on faults in the Imperial  
804 Valley triggered by the 4 April 2010 Mw 7.2 El Mayor-Cucapah earthquake revealed by  
805 InSAR, *Geophysical Research Letters*, 38(January), 1–6, doi:10.1029/2010GL045235.
- 806 Wei, M., Y. Liu, Y. Kaneko, J. J. McGuire, and R. Bilham (2015), Dynamic triggering of  
807 creep events in the Salton Trough, Southern California by regional M5.4 earthquakes  
808 constrained by geodetic observations and numerical simulations, *Earth and Planetary*  
809 *Science Letters*, 427, 1–10, doi:10.1016/j.epsl.2015.06.044.
- 810 Wei, S., E. Fielding, S. Leprince, A. Sladen, J.-P. Avouac, D. Helmberger, E. Hauksson,  
811 R. Chu, M. Simons, K. Hudnut, T. Herring, and R. Briggs (2011b), Superficial sim-  
812 plicity of the 2010 El MayorCucapah earthquake of Baja California in Mexico, *Nature*  
813 *Geoscience*, 4(9), 615–618, doi:10.1038/ngeo1213.
- 814 Yang M., and M. N. Toksöz (1981), Time-dependent deformation and stress relaxation  
815 after strike-slip earthquakes, *Journal of Geophysical Research*, 86, 2889–2901.
- 816 Yuen, D. A., and W. R. Peltier (1982), Normal modes of the viscoelastic earth, *Geo-  
817 physical Journal of the Royal Astronomical Society*, 69, 495–526, doi:10.1111/j.1365-  
818 246X.1982.tb04962.x.